Draft version July 2, 2023
Typeset using LaTeX **twocolumn** style in AASTeX63

Corotating Clumps Around Adolescent Low-Mass Stars: Four Years of TESS

Author list and order not final!,[1] Luke G. Bouma,[1,*] Rahul Jayararaman,[2] Saul Rappaport,[2]
Lynne A. Hillenbrand,[1] George R. Ricker,[2] and Gáspár Á. Bakos[3]

[1]*Department of Astronomy, MC 249-17, California Institute of Technology, Pasadena, CA 91125, USA*
[2]*MIT Kavli Institute and Department of Physics, 77 Massachusetts Avenue, Cambridge, MA 02139*
[3]*Department of Astrophysical Sciences, Princeton University, 4 Ivy Lane, Princeton, NJ 08540, USA*

(Received —; Revised —; Accepted —)

ABSTRACT

Complex quasiperiodic variables (CQVs) are low-mass pre-main-sequence stars with nearly periodic optical modulation. The modulation is likely induced by dust or gas clumps in orbit at the Keplerian corotation radius. Here, we report new CQVs discovered in TESS data collected between July 2018 and Sep 2022. Our search of 65,760 K- and M-dwarfs with $T<16$ and $d<150$ pc yielded 53 gold-standard CQVs. Most of these discoveries are new, and they include the brightest and closest examples of this class of object known ($T\approx9.5$; $d\approx20$ pc), as well as the most massive ($\approx0.65\,M_\odot$). A few objects are outliers among outliers; LP 12-502 for instance shows a "dip complex" with a period and total duration that are fixed over more than 1,000 cycles, but which in detail exhibits anywhere from four to eight local minima per cycle. LP-502 also displayed distinct superposed periods simultaneously, and displayed drastic shape changes shortly after flares. Broadly speaking, we find that none of the CQVs maintain a fixed light curve shape over timescales of more than a few hundred cycles, and we revisit the arguments for why transient corotating material is the most viable explanation. In the future, we expect that our sample will facilitate modeling and observational efforts aimed at understanding these objects, and connecting them to the broader contexts of star, disk, and exoplanet evolution. For instance, if the transiting material is dust, then the rate of dip evolution implies that of order an asteroid belt's worth of mass passes through these structures over the 10^8 years for which they are observed.

Keywords: Weak-line T Tauri stars (1795), Periodic variable stars (1213), Circumstellar matter (241), Star clusters (1567), Stellar magnetic fields (1610), Stellar rotation (1629)

1. INTRODUCTION

All pre-main-sequence stars vary in optical brightness, and the origin of such variability is, in most cases, understood. Well-explored sources of optical variability include inhomogeneities on stellar surfaces such as starspots and faculae (Basri 2021), occultations by gas-rich circumstellar disks (Bodman et al. 2017), and, in geometrically favorable circumstances, eclipses by stars and planets (Winn 2010). More exotic forms of optical variability relevant to this work include transiting exocomets (e.g. β Pic; Zieba et al. 2019) and disintegrating rocky bodies around both M-dwarfs (e.g. KOI-2700; Rappaport et al. 2014) and white dwarfs (e.g. WD 1145; Vanderburg et al. 2015).

Data from K2 and TESS have yielded a new class of variable star whose root cause is only beginning to become clear: complex quasiperiodic variables (CQVs). These objects are identified phenomenologically using their optical light curves, which show nearly periodic troughs that can be either sharp or broad, often superposed on smooth spot-like modulation (Stauffer et al. 2017, 2018; Zhan et al. 2019). Some CQVs show up to eight local minima (dips) per cycle. Most are pre-main-sequence M-dwarfs without near-infrared excesses, ages of ≈5-150 million years (Myr), and rotation periods of at most two days; they are observed to be ≈1-3% of M-dwarfs younger than 100 Myr (Rebull et al. 2016; Günther et al. 2022). The dips can be chromatic, with a reddening law plausibly consistent with dust (Bouma et al. 2020; Günther et al. 2022; Koen 2023). And finally, while the dip shapes can "jump" between different depths and durations over less than one cycle, they more often evolve gradually, over tens to hundreds of cycles (e.g. Stauffer et al. 2017; Palumbo et al. 2022; Popinchalk et al. 2023).

A few competing explanations for what causes the complex quasiperiodic variability are shown in Figure 1, along with some representative light curves. All young M-dwarfs are spotted, which produces flux variations over characteristic timescales of the rotation period, $P_{\rm rot}$, and its half-harmonic, $0.5\,P_{\rm rot}$. The observed dips occur over durations

Corresponding author: Luke G. Bouma
luke@astro.caltech.edu

* 51 Pegasi b Fellow

as short as $0.05\,P_{\rm rot}$; a "starspot-only" scenario can be discarded for any object with sufficiently sharp dips (Stauffer et al. 2017; Koen 2021). The timescales and amplitudes of the flux variations instead require sharp geometries with material extrinsic to the stellar surface (e.g. Stauffer et al. 2017; Günther et al. 2022). The "clump" scenario invokes opaque dust clumps orbiting near the Keplerian corotation radius, which periodically eclipse the star (Stauffer et al. 2017; Sanderson et al. 2023). The "prominence" scenario invokes long-lived condensations of cool and dense marginally-ionized gas, embedded within the hotter corona, that would be centrifugally supported near corotation (Collier Cameron & Robinson 1989; Jardine & Collier Cameron 2019; Waugh & Jardine 2022). Such structures are analogous to quiescent prominences and filaments observed in the solar corona (see e.g. 201 2015), though at much larger relative distances from the stellar surface. A final posibility that has been suggested is one of a "screen", in which the inner wall of a quiescent circumstellar disk blocks a portion of the stellar surface to produce sudden dips whenever spots come into view (Zhan et al. 2019).

The dust clump and prominence hypotheses seem most plausible. They are qualitatively similar, except that one invokes opacity from dust, while the other invokes opacity from gas, likely bound-free transitions in hydrogen or perhaps a molecular opacity. The screen scenario seems inconsistent with the degree of observed periodicity, the lack of infrared excess, and the observed lifetime of CQVs extending an order of magnitude longer than the $\approx 10^7$ year timescale typically quoted for the primordial disk to disperse. However, unambiguous evidence has yet to be acquired in support of any scenario. Such evidence might include a spectroscopic detection of silicate $10\,\mu$m dust absorption during a dip, or perhaps detection of transient Balmer-line absorption during the dips, similar to observations made in systems such as AB Dor (see the review by Collier Cameron 1999).

CQVs remain mysterious because they have been both hard to discover and hard to characterize. Discoverability is tied to rarity: CQVs comprise about 1% of the youngest 1% of M-dwarfs (Rebull et al. 2018). Out of the millions of stars monitored by K2 and TESS, about 50 CQVs have been reported to date (Rebull et al. 2016; Stauffer et al. 2017, 2018; Zhan et al. 2019; Bouma et al. 2020; Günther et al. 2022; Popinchalk et al. 2023). The known CQVs are correspondingly faint; the initial K2 discoveries (Rebull et al. 2016; Stauffer et al. 2017) were M2-M6 dwarfs at distances $\gtrsim$100 pc, yielding optical brightnesses of $V\approx15.5$ to $V>20$. This renders time-series spectroscopy at high resolution technically impossible, despite its potential utility in ruling between the models.

One way to help rule between the mechanisms is to therefore find bright and nearby CQVs, since these objects will be the most amenable to detailed photometric and spectroscopic analyses. To do this, in this work, we use 120-second cadence data acquired by TESS between July 2018 and Sep 2022 (Sectors 1-55; Cycles 1-4). We present our search methods in Section 2, and the properties of the resulting CQV catalog in Section 3. The evolution of many CQVs over a two-year baseline is described in Section 4, including a deep-dive into LP 12-502. Implications are discussed in Section 5, and we conclude in Section 6.

A word on nomenclature. CQVs have been called "transient and persistent flux dips", "scallop shells", "batwings", (Stauffer et al. 2017) "complex rotators", (Zhan et al. 2019; Günther et al. 2022; Popinchalk et al. 2023) and "complex periodic variables" (Koen 2023). The CQVs should not be conflated with "dippers", which are classical T Tauri stars with infrared excesses whose optical variability is linked to obscuring inner disk structures and accretion hot spots (Cody et al. 2014; Robinson et al. 2021). At the risk of introducing yet another standard, we prefer a nomenclature that reflects how, when observed over timescales of more than tens of cycles, CQVs are almost but not exactly periodic. They are irregularly periodic, or for short, quasiperiodic. While the three-type classification scheme proposed by Stauffer et al. (2017) may indeed provide some helpful visual distinctions amongst CQV sub-classes, it seems likely that they are all explained by a single underlying phenomenon, and so we opt to refer to them by a single empirically descriptive name.

2. METHODS

2.1. *Stellar selection function*

We analyzed the "short" 120-second cadence data acquired by TESS between July 2018 and Sep 2022 (Sectors 1-55). Specifically, we used the 120-second cadence light curve products produced by the mission's Science Processing and Operations Center at NASA Ames (Jenkins et al. 2016). While the TESS data products also include full frame images with cadences of 200, 600, and 1800 seconds, we limited our scope in this work for the sake of simplicity in data handling. In exchange, we lose in both completeness and homogeneity of the selection function. While TESS cumulatively observed $\approx$90% of the sky for at least one lunar month between July 2018 and Sep 2022, the 120-second cadence data were acquired for only a pre-selected set of stars over Sectors 1-26, and then a guest-investigator driven set of stars over Sectors 27-55 (Fausnaugh et al. 2021).

To assess the completeness of the resulting 120-second cadence data that is the basis of this study, we cross-matched TIC8 (Stassun et al. 2018) against the Gaia DR2 point-source catalog (Gaia Collaboration et al. 2018). We opted for Gaia DR2 rather than DR3 because the base catalog for TIC8 was Gaia DR2, which facilitated a one-to-one crossmatch using the Gaia source identifiers. This exercise showed that for $T<16$ M-dwarfs, the TESS 2-minute data are roughly 50% complete at $\approx$50 pc. At $<$20 pc, $\gtrsim$80% of the $T<16$ M-dwarfs have at least one sector of short-cadence data; at $>$100 pc, $\lesssim$10% of such M-dwarfs have at least one sector of short-cadence data. Armed with this understanding, we then used our cross-match between Gaia DR2 and TIC8 to select our stars of interest, which we defined as stars with

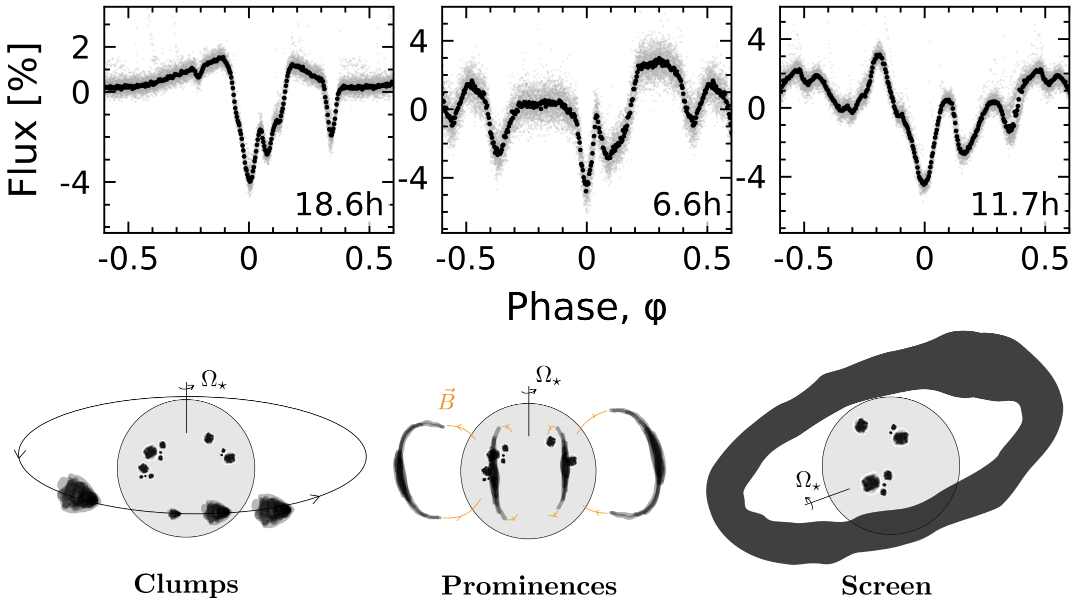

Figure 1. **Complex quasiperiodic variables (CQVs)**: *Top:* Phase-folded TESS light curves of three CQVs. Each is stacked over one month. Gray are raw 2-minute data; black bins to 300 points per cycle. Periods in hours are in the bottom right of each panel. In order left-to-right, the objects are LP 12-502 (TIC 402980664; Sector 19), TIC 94088626 (Sector 10), and TIC 425933644 (Sector 28). *Bottom:* Plausible cartoon models for the phenomenon. The dust clump scenario seems most plausible, given the stability of the dips, their chromaticity, the lack of observed infrared excesses, and the challenge of producing broadband opacity variations with only ionized hydrogen in the prominence scenario.

120-second cadence TESS light curves that satisfied

$$T < 16 \quad \text{(Bright for TESS)} \tag{1}$$
$$G_{\rm BP} - G_{\rm RP} > 1.5 \quad \text{(Red stars only)} \tag{2}$$
$$M_{\rm G} > 4 \quad \text{(Dwarf stars only)} \tag{3}$$
$$d < 150\,\text{pc} \quad \text{(Close stars only)}, \tag{4}$$

for $M_{\rm G} = G + 5\log(\varpi_{\rm as}) + 5$ the Gaia G-band absolute magnitude, $\varpi_{\rm as}$ the parallax in units of arcseconds, and a geometric distance d defined by inverting the parallax and ignoring any zero-point correction. This selection function includes dwarf stars later than spectral types of ≈K6V (Pecaut & Mamajek 2013) for which TESS can acquire 1% relative precision photometry in 1 hour of observation (Ricker et al. 2015). The target sample therefore includes 65,760 M-dwarfs and late-K dwarfs, down to $T<16$ and out to $d<150$ pc.

2.2. *CQV discovery*

Previous methods for finding CQVs have included visually examining stars known to be in young clusters (Rebull et al. 2016; Stauffer et al. 2017), and automatically flagging rapid rotators with a large number of strong Fourier harmonics (Zhan et al. 2019). The latter approach still requires visual vetting, since "stars with many Fourier harmonics" is a designation that includes objects such as eclipsing binaries or multiple stars blended into a single photometric aperture. In this work, we implemented a new search approach based on counting the number of sharp local minima in phase-folded light curves, while also using the previously tested Fourier approach. We applied these two search techniques independently.

2.2.1. *Counting dips*

The dip counting technique aims to count sharp local minima in phase-folded light curves. CQVs will preferably have at least three such minima in order to be distinct from false positives such as synchronized and spotted binaries ("RS CVn" stars).

For our dip-counting pipeline, we began with the PDC_SAP flux for each sector, removed non-zero quality flags, and normalized the light curve to one by dividing out its median value. We then flattened the light curve using a 5-day sliding median filter, as implemented in `wotan` (Hippke et al. 2019). On the resulting cleaned and flattened light curve, we ran a periodogram search, opting for the Stellingwerf (1978) phase dispersion minimization (PDM) algorithm implemented in `astrobase` (Bhatti et al. 2021) due to its shape agnosticism. If a period below 2 days was identified, we reran the periodogram at a finer grid to improve the accuracy of the period determination.

Once a star's period P was identified, we binned the phased light curve to 100 points per cycle. To separate "sharp" local minima from smooth spot-induced variability, we then iteratively fit penalized splines to the wrapped phase-folded light curve, excluding points more than two standard deviations away from the local continuum (Hippke et al. 2019). The maximum number of equidistant spline knots per cycle is the parameter in this framework that controlled the meaning of "sharp" — we allowed at most 10 such knots per cycle, though for most stars fewer knots were preferred based on an ℓ^2-norm penalty.

We then identified local minima in the resulting residual light curve using the SciPy `find_peaks` utility (Virtanen et al. 2020), which is based on comparing adjacent values in an array. For a peak to be flagged as significant, we required it to have a width of at least $0.02P$, and a height of at least twice the point-to-point RMS. This latter quantity is defined as the 68$^{\rm th}$ percentile of the distribution of the residuals from the median value of $\delta f_i \equiv f_i - f_{i+1}$, where f is the flux and i is an index over time.

To correctly identify local minima near the edges of the phased light curve, which usually would cover phases $\phi \in [0,1]$, we in fact performed the entire procedure over a phase-folded light curve spanning $\phi \in [-1,2]$, by duplicating and concatenating the ordinary phase-folded light curve. The free parameters we adopted throughout this analysis procedure, for instance the maximum number of spline knots per cycle, and how large and wide of a local minimum to consider a "true dip", were chosen during a testing period based on their ability to correctly re-identify a large fraction (>90%) of known CQVs, while also being able to consistently reject common false positives such as rapidly rotating spot-induced variability and typical eclipsing binaries.

Overall, for a star to clear this process and to proceed to manual examination, we required that it have a peak PDM period below two days, and that it exhibited at least three sharp local minima (as algorithmically reported) in at least one observed TESS sector.

2.2.2. *Fourier analysis*

For the Fourier analysis, we followed Zhan et al. (2019).

TODO for Rahul or Saul: explain the approach, in a few paragraphs. Was the SAP_FLUX or PDCSAP used? etc.

2.2.3. *Manual vetting*

We visually assessed whether the objects found using the Fourier (Section 2.2.2) and dip-counting (Section 2.2.1) techniques were consistent with expectations for CQVs by assembling the data shown in Appendix A. We labelled a star as a "good" CQV if at least one TESS sector showed what we viewed as the unambiguous signatures of the class (short period; at least three dips or else otherwise oddly-shaped dips; relative stability over a timescale of 30 days). We also noted stars that we thought could be CQVs, but that were more ambiguous with a "maybe" flag.

Broadly speaking, the most common false positives for both the Fourier and dip-counting techniques were eclipsing binaries, spot-induced variability from rapid rotators, and variability from neighboring, off-target stars. Typical false postive rates from our dip-counting pipeline were 5:1, with 368 unique stars flagged, and about 20% being labelled either "good" or "possible" CQVs; for the Fourier pipeline, **the rate was X:Y, with ZZZZ unique stars flagged, and NN% being labelled "good" or "possible" CQVs**.

2.3. *Stellar properties*

Ages—We estimated the stellar ages by making probabilistic spatial and kinematic associations between the CQVs and known clusters in the solar neighborhood. For most stars in our sample, we did this using BANYAN Σ (Gagné et al. 2018).[1] This algorithm calculates the probability that a given star belongs to one of 27 young clusters (or "associations") within 150 pc of the Sun, by modeling the clusters as multivariate Gaussians in 3-D position and 3-D velocity space. We used the Gaia DR2 sky positions, proper motions, and distances to calculate the membership probabilities. BANYAN Σ in turn analytically marginalizes over the radial velocity dimension. The probabilities returned by this procedure are qualitatively useful, but we emphasize that they are quantitatively dubious due to the non-Gaussian nature of most groups within the solar neighborhood (see e.g. Kerr et al. 2021, Figure 10).

For a few cases where BANYAN Σ yielded ambiguous results, we consulted the meta-catalog of young, age-dated, and age-dateable stars within a kiloparsec from Bouma et al. (2022), and also searched the local volume around each star for co-moving companions.[2]

Effective temperatures, radii, and masses—We determined the stellar effective temperature and radii through SED fitting; we then estimated the masses by interpolating against the PARSEC v1.2S models (Bressan et al. 2012; Chen et al. 2014).

For the SED fitting, we used `astroARIADNE` (Vines & Jenkins 2022). We adopted the "BT-Settl" stellar atmosphere models (Allard et al. 2012) assuming the Asplund et al. (2009) solar abundances, and the Barber et al. (2006) water line lists. The broadband magnitudes we considered included $GG_{\rm BP}G_{\rm RP}$ from Gaia DR2, $Vgri$ from APASS, $JHK_{\rm S}$ from 2MASS, SDSS riz, and the WISE 1-2 passbands. We specifically omitted UV flux measurements to avoid biasing our fit with any possible chromospheric UV excess. `astroARIADNE` compares the measured broadband flux measurements against pre-computed model grids, and by default fits for six parameters: $\{T_{\rm eff}, R_\star, A_{\rm V}, \log g, [{\rm Fe/H}], d\}$. The distance prior is drawn from Bailer-Jones et al. (2021). The surface gravity and metallicity are generally unconstrained. And finally, given our particular use-case, we assumed the following priors for the temperature, stellar size, and extinction:

$$T_{\rm eff}/{\rm K} \sim \mathcal{N}(3000, 1000), \tag{5}$$
$$R_\star/{\rm R}_\odot \sim \mathcal{T}_{\rm N}(0.5, 0.3, 0.1, 1.5), \tag{6}$$
$$A_{\rm V}/{\rm mag} \sim \mathcal{U}(0, 0.2), \tag{7}$$

for $\mathcal{N}$ the Gaussian and $\mathcal{U}$ the uniform distributions, and $\mathcal{T}(\mu, \sigma, a, b)$ a truncated normal distribution with mean μ, standard deviation σ, and lower and upper bounds a and b.

[1] https://github.com/jgagneastro/banyan_sigma, git commit `394b486`

[2] https://github.com/adamkraus/Comove, git commit `278b372`

Using `Dynesty` (Speagle 2020), we statically sampled the posterior probability assuming the default Gaussian likelihood, and set a stopping threshold of $d\log\mathcal{Z} < 0.01$, where $\mathcal{Z}$ denotes the evidence.

With the effective temperatures and stellar radii from the SED fit, we then estimated the stellar masses by interpolating against the PARSEC isochrones (v1.2S Chen et al. 2014). The need for models that incorporate some form of correction for young, active M-dwarfs is well-documented (e.g. Stassun et al. 2012; David & Hillenbrand 2015; Feiden 2016; Somers et al. 2020). Plausible explanations for anomalous M-dwarf colors and sizes relative to model predictions include star starspot coverage (e.g. Gully-Santiago et al. 2017), and potentially incomplete line lists (e.g. Rajpurohit et al. 2013). In the PARSEC models, Chen et al. (2014) performed an empirical correction to the temperature–opacity relation drawn from the BT-Settl model atmospheres, in order to match observed masses and radii of younq eclipsing binaries. This is sufficient for our purpose of estimating accurate stellar masses. Given our observed $\{\tilde{T}_{\rm eff}, \tilde{M}_\star, \tilde{t}\}$, and approximating their uncertainties as Gaussian $\sigma_{\tilde{T}_{\rm eff}}$, $\sigma_{\tilde{M}_\star}$ and $\sigma_{\tilde{t}}$, we evaluate a distance d between our observations and any model PARSEC grid-point $\{T_{\rm eff}, M_\star, t\}$ as

$$d^2 = \left(\frac{\tilde{T}_{\rm eff} - T_{\rm eff}}{\sigma_{\tilde{T}_{\rm eff}}}\right)^2 + \left(\frac{\tilde{M}_\star - M_\star}{\sigma_{\tilde{M}_\star}}\right)^2 + \left(\frac{\tilde{t} - t}{\sigma_{\tilde{t}}}\right)^2, \quad (8)$$

in order to assign equal importance to each dimension. The preferred model mass is then one that minimizes this distance, and is quoted in Table **??**.

3. RESULTS

3.1. *CQV catalog*

Table **??** lists the 70 CQVs identified by our search, along with important physical and observational properties. 53 objects demonstrated what we viewed as unambiguous characteristics of the CQV phenomenon in at least one TESS sector; we refer to these as the "gold sample". We found the remaining 17 CQV candidates to be ambiguous; their variability might be caused by say, multiple starspot groups. Additional data from TESS or other instruments could help resolve their classification. In the following discussion, we will primarily restrict our discussion to the gold sample.

The mosaic in Figure 2 shows phased light curves for the 53 bonafide CQVs. The objects are sorted first in order of the number of TESS 120-second cadence sectors in which they clearly demonstrated the CQV phenomenon, and secondarily by descending brightness. The objects at the top generally have the most 120-second cadence data. The top five objects by this metric are TIC 300651846 (T=13.5, 12 sectors); TIC 402980664 (T=11.1, 7 sectors); TIC 89463560 (T=13.5, 5 sectors); TIC 363963079 (T=12.9, 5 sectors); and TIC 294328887 (T=14.2, 4 sectors). The brightest five CQVs span $9.3<T<11.1$; the faintest five span $14.5<T<15.0$. The fastest five have periods spanning 3.6 hr$<P<$6.2 hr, while the slowest five span 27 hr$<P<$38 hr.

In terms of the light curve shapes, Figure 2 shows a broad range of variability, with anywhere from two to eight local minima per cycle. Some stars show relatively ordinary modulation during one continuous portion of the phased light curve, and highly structured modulation in the remainder of the cycle (e.g. TIC 206544316, TIC 224283342, TIC 402980664). Others show structured modulation over the entire span of a cycle (e.g. TIC 2234692, TIC 401789285, TIC 425933644, TIC 142173958). Others still show some mix between these two modes.

A small number of objects at first glance seem reminiscent of eclipsing binaries, such as TIC 193831684 or TIC 5714469. In these few cases, we believe that that are unlikely to be eclipsing binaries due to additional coherent variations in the light curves that are distinct from any binary phenomenology of which we are aware.

3.2. *Ages*

Of our 70 confirmed and candidate CQVs, 67 were associated with a nearby moving group or open cluster using BANYAN Σ. The relevant groups are listed in Table **??**; their ages span ≈5-150 Myr. The most prodigious groups were Sco-Cen, Tuc-Hor, and Columba. The yield in Sco-Cen is not particularly surprising, since Sco-Cen contains the majority of pre-main-sequence stars in the solar neighborhood. However it is certainly likely given the $\lesssim$10% completeness of TESS beyond 100 pc that far more CQVs remains to be discovered in Sco-Cen. IC 2602 and IC 2391, which are located slightly beyond 100 pc, are an example of this completeness effect: no CQVs appear in those clusters from our search.

Of the three stars for which BANYAN Σ did not find any association, one (TIC 302160226) is a member of α Per ($t \approx 86 \pm 16$ Myr; Meingast et al. 2021; Boyle & Bouma 2023). For the other two (TIC 58084670 and TIC 141146667), we were not able to confidently associate either star with any young groups. However both do seem to clearly show the CQV signal over multiple TESS sectors, and both are photometrically elevated relative to the main sequence. For instance, both were noted as being in the "diffuse" Class III YSO population near the Sun by Kerr et al. (2021).

Our catalog confirms that the CQV phenomenon persists for at least ≈150 Myr. Our catalog includes three ≈150 Myr CQVs in AB Dor (Bell et al. 2015): TIC 288344202, TIC 332517282, and TIC 368129164. There is also a ≈112 Myr old Pleiades CQV (TIC 440725886; Dahm 2015; Cantat-Gaudin et al. 2020), and a similarly-aged Psc-Eri member (TIC 38539720; Ratzenböck et al. 2020). To our best knowledge, TIC 332517282 was the previous record-holder for oldest-known CQV (Zhan et al. 2019; Günther et al. 2022); at least one unambiguous case (EPIC 211070495) and a few other candidates were also previously known in the Pleiades (Rebull et al. 2016). While we expect to have been sensitive to CQVs in the nearby Hyades (≈700 Myr), again due to the specifics of the TESS 120-second selection function, we do not know at this time whether we would have been sensitive to such stars.

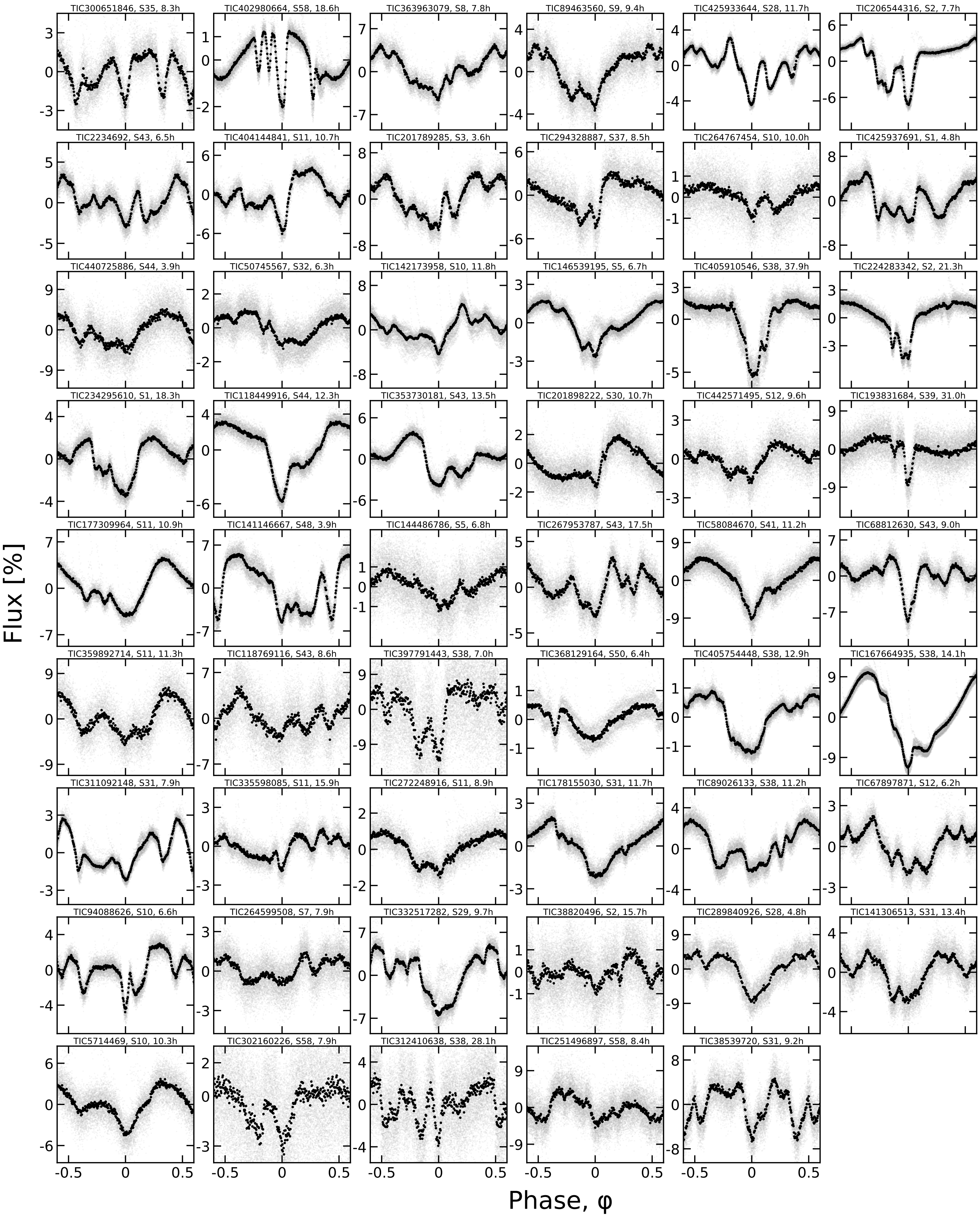

Figure 2. CQVs found in the TESS 2-minute data. Phased TESS light curves over one month are shown for 53 CQVs. Gray are raw 2-minute data; black bins to 300 points per cycle. Each panel is labelled by the TIC identifier, the TESS sector number, and the period in hours. Objects are ordered such that sources with the most TESS data available are on top (see Section 3.1).

Finally, six CQVs were identified in the recently confirmed Argus association (Zuckerman 2019). This serves as an indirect line of evidence supporting the reality, and youth, of that group.

3.3. *Infrared excesses*

As is typical for CQVs (Stauffer et al. 2017), most CQVs in our catalog did not show infrared excesseses in the WISE1-4 bands. Visually inspecting the SEDs of our entire 70 star sample, we labelled two objects as having "good" infrared excesses (both W3 and W4), and three as "possible" infrared excess.

The two "good" IR excesses belonged to "candidate" CQVs TIC 193136669 (TWA 34) and TIC 57830249 (TWA 33). Both are in the TW Hydrae association ($\approx$10 Myr), and have relatively long periods of 38 hr and 44 hr respectively. In our initial labelling, we labelled both as "maybe" CQVs because the dips in their light curves did not show the rigid periodicity typical of CQVs; their periods were also relatively long. After labelling them, inspection of further sectors clarified that both sources are dippers (see plots in Appendix A). In addition, TIC 193136669 has a cold molecular disk based on observed 1.3 mm continuum emission and resolved Keplerian ^{12}CO(2−1) emission (Rodriguez et al. 2015). It was also labelled a dipper by Capistrant et al. (2022); we agree with their designation, but nonetheless leave it in our catalog as an indication of possible ambiguities in our search process. TIC 57830249 (TWA 33) also has previously detected 1.3 mm continuum emission (Rodriguez et al. 2015), suggestive of cold dust grains being present. It therefore also a dipper that snuck its way into our "maybe" pile. Possible evolutionary connections between CQVs and dippers are highlighted in Section 5.6.

Our three "possible" infrared excesses were TIC 405910546, 289840926, and 244161191. After a literature search, we concluded that none have clear evidence for the presence of a disk. TIC 405910546, in LCC, shows a unique TESS light curve, reminescent of a P=38 hr singly-eclipsing binary, except with additional substructure during each eclipse that resembles the CQV phenomenon more than any other variability of which we are aware. TIC 289840926 (β Pic moving group, P=4.8 hr), show what we believe is a clear CQV signals, but has no definitive evidence for a large, dusty disk. TIC 244161191 (hilariously, TOI-278), in Columba, also has no definitive evidence for a large disk. It is however "multi-periodic"—in addition to the 7.17 hr CPV signal, this source shows a superposed 8.39 hr sinusoidal signal, probably from an unresolved neighboring star.

4. CQV EVOLUTION

4.1. *Evolution over two year baseline*

Figure 3 shows "before" and "after" views of 27 CQVs for which TESS 120-second cadence observations were available at least two years apart. Such a baseline was available for 32 of the confirmed 53 CQVs in our catalog; for plotting purposes we show the brightest 27. Of these 27 CQVs, a few show clear signs of the phenomenon in one sector, and marginal or non-existence signs in the other. While there is some subjectivity in this assessment, to our eyes cases for which at least one sector would be flagged as "ambiguous" include TIC 368129164 (Sector 23 might be labelled an EB), TIC 177309964 (Sector 38 would be simply a rotating star), TIC 404144841 (Sector 38 looks like a rotating star), TIC 201898222 (Sector 3 looks like a rotating star), TIC 144486786 (Sector 32 might be an RS CVn), and TIC 38820496 (Sector 28 might be an RS CVn). TIC 193831684, assessed on a single-sector basis, would probably be labelled an eclipsing binary—in fact, Justesen & Albrecht (2021) implicitly have already given this source such a label. However, based on the the shape evolution between Sectors 13 and 39, it is a CQV. One could easily also imagine in cases like TIC 206544316 that if observed at lower signal to noise, the drastic shape evolution would not be appreciated. We emphasize that the periods themselves were all stable to $<$0.1%. Broadly speaking, this shape evolution suggests that CQVs have an "on/off" duty cycle of $\approx$75%. This type of correction is likely worth including in population-level estimates of how intrinsically common CQVs are in the low-mass stellar population (e.g. Günther et al. 2022).

4.2. *Evolution over adjacent sectors, & LP 12-502*

4.2.1. *LP 12-502 observations*

While many CQVs had multiple sectors of adjacent or nearly-adjacent data, LP 12-502 (TIC 402980664; d=21 pc, J=9.4, T=11.1) stood out due to the quality and content of its data. Figure 4 shows all available data from Sectors 18, 19, 25, 26, 53, 58, and 59, split into successive orbits; the star was observed at 120-second cadence whenever it was observable by TESS. We binned the light curve to 15-minute intervals for visual clarity, and required at least one (120-second cadence) flux measurement per bin. Points more than 2.5σ above the median are drawn in gray, also for visual clarity. Missing data are not drawn. Figure 5 then shows the same data, but stacked into successive TESS orbits spanning half a lunar month each.

The average period, determined by measuring the PDM peak period over each sector independently, was $\langle P \rangle$ = 18.5560 hr. The range between the maximum and minimum sector-specifics periods was measured to be about one minute. Based on this range, the star's period is stable to at least one minute ($\pm$0.017 hr) over the three year baseline. However, in detail, a period shift of $\pm$1 minute would yield major phase drifts over the baseline; that time interval corresponds to roughly 1/1000$^{\text{th}}$ of a period, and we have observed 1500 cycles. The achievable period precision, $\sigma_{\rm P}$, can be estimated as

$$\sigma_{\rm P} = \frac{\sigma_\phi P}{N_{\rm baseline}}, \tag{9}$$

for $N_{\rm baseline}$ the number of cycles in the observed baseline and σ_ϕ the phase precision with which any one feature (e.g. a dip, or the overall shape of the sinusoidal envelope) can be tracked. Assuming $\sigma_\phi \approx 0.01$ yields an expected period precision $\sigma_{\rm P} \approx 0.45\,{\rm sec} \approx 1.2 \times 10^{-4}\,{\rm hr}$. By visually

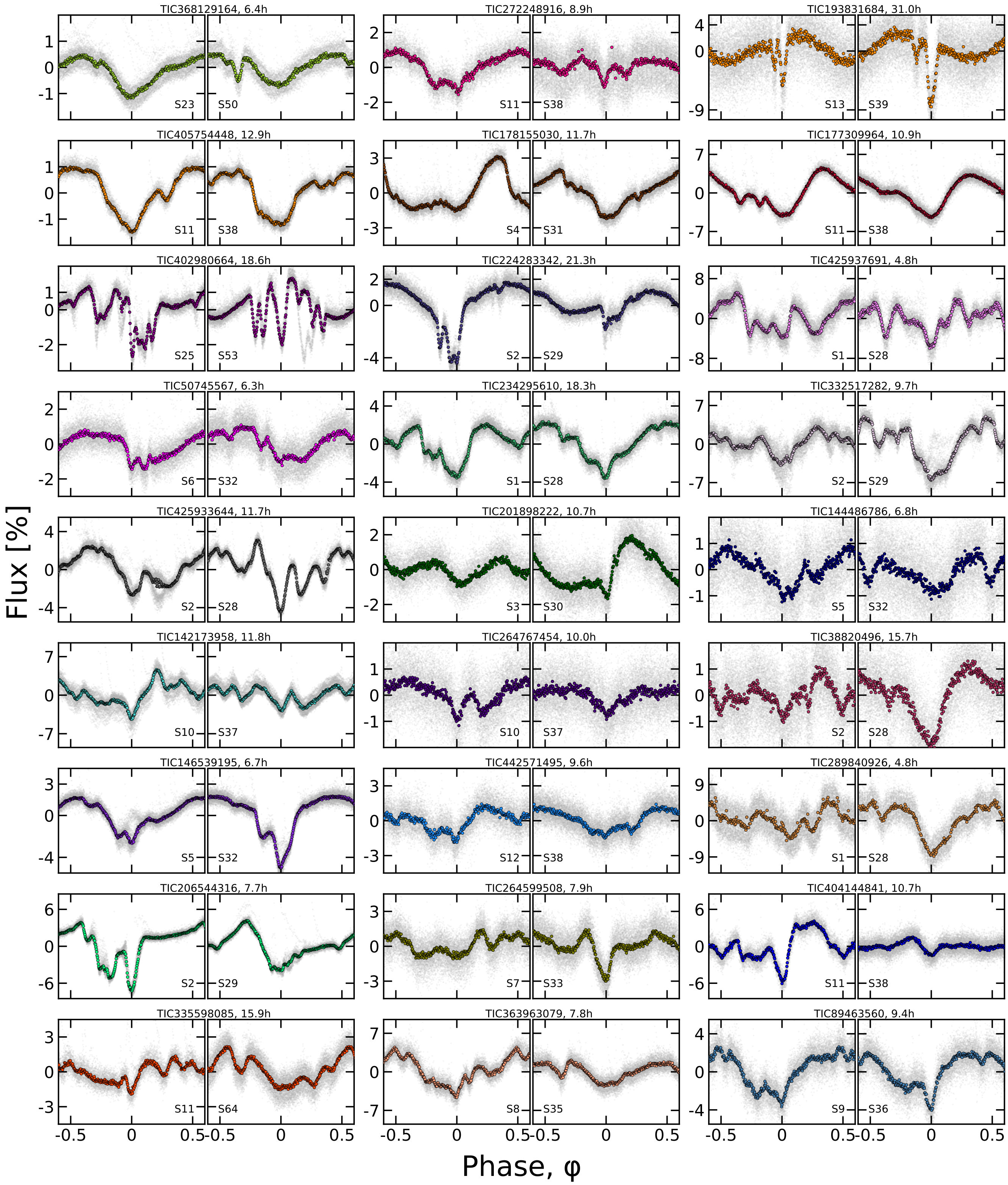

Figure 3. CQVs keep their periods but change their shapes. 32 of our 53 CQVs from Figure 2 had 120-second cadence TESS data available for a baseline of at least two years; the 27 brightest are shown here. Each panel shows one sector of TESS data, and is phased to its deepest minimum in flux. Each panel's title shows the TIC identifier and approximate period in hours. Text insets show the TESS sector numbers, which generally span two years, or at least 1,000 cycles. The vertical scale is fixed across sectors to clarify shape changes.

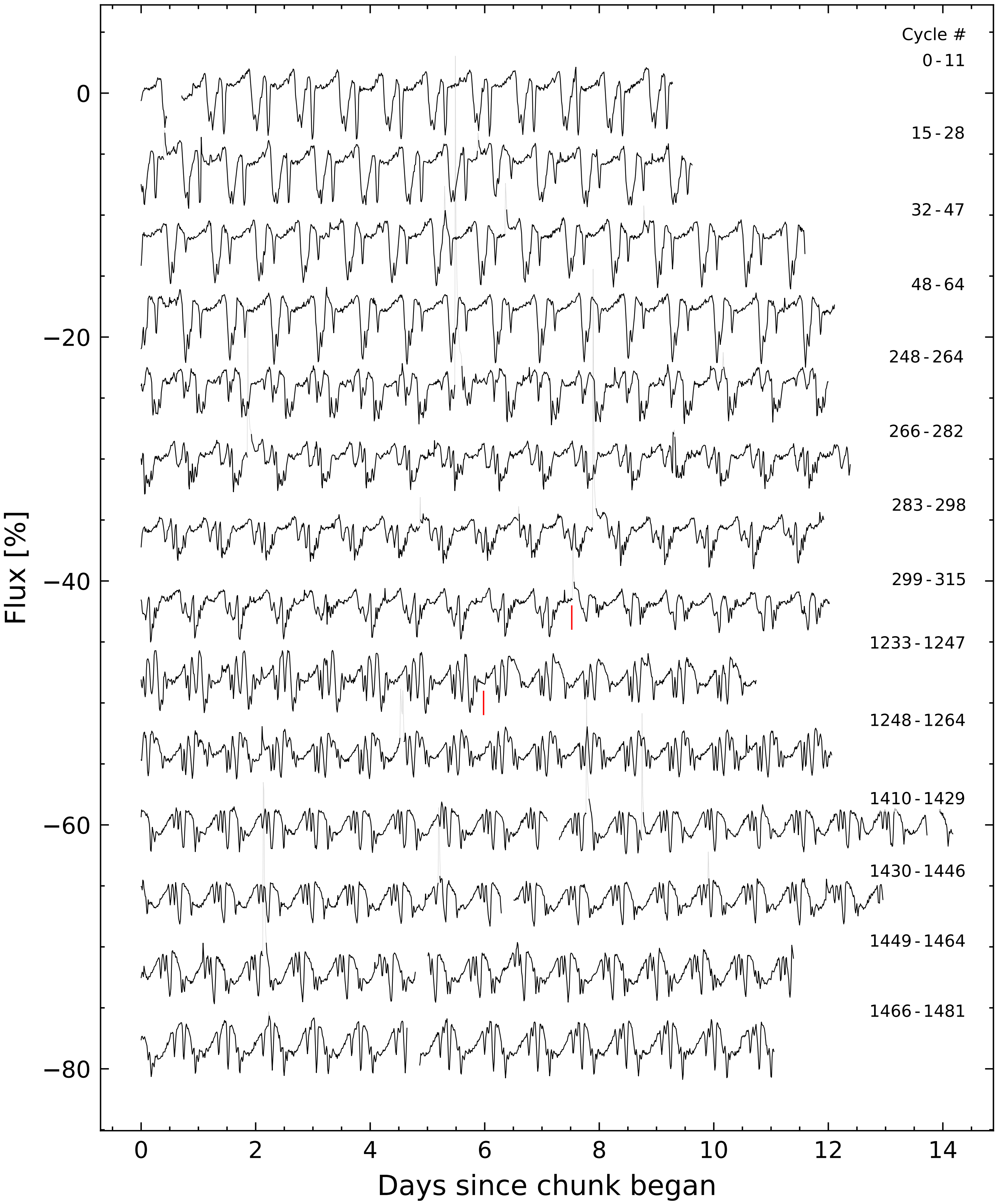

Figure 4. LP 12-502 (TIC 402980664) light curve, where each time chunk represents one TESS orbit. Data were acquired in Sectors 18-19, 25-26, 53, and 57-58. Flares are drawn in gray. The red vertical lines highlight apparently instantaneous state changes in the shape of the dip pattern. The light curve is binned to 15-minute intervals so that there are 96 points per day. Data gaps with more than one missing 15-minute cadence appear in white.

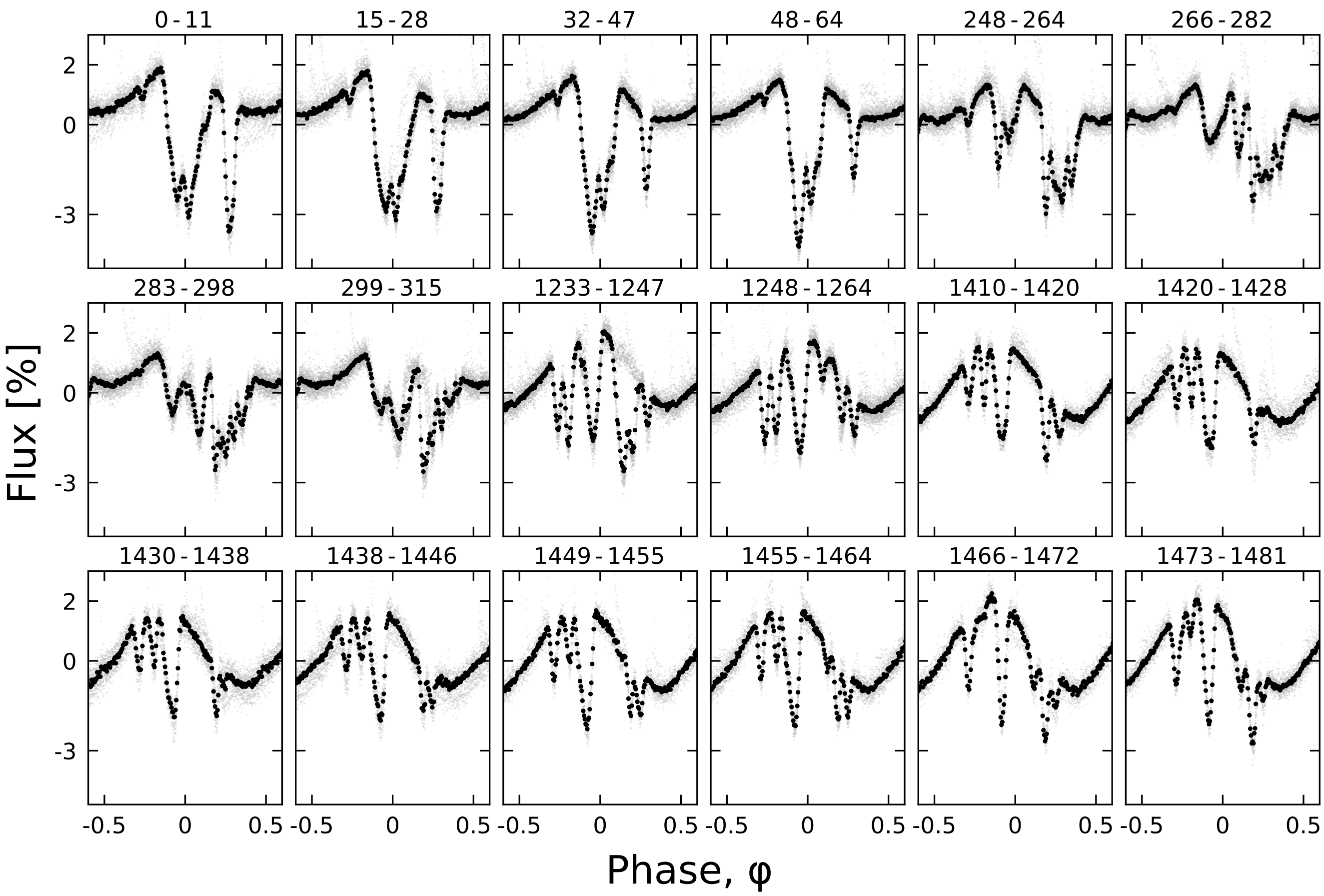

Figure 5. Evolution of LP 12-502 (P=18.6 h) at fixed period and epoch over three years. Each panel shows one (stacked) TESS orbit; small text denotes relative cycle number. There are 200 binned black points per cycle. The TESS pointing law dictates time gaps; larger gaps tend to yield larger shape changes. The dips usually evolve over tens to hundreds of cycles. However cycles 1233-1264 show a dip that "switched" from a depth and duration of 3% and 3 hr to 0.3% and 1 hr over less than one cycle (cf. Figure 4).

fine-tuning over a grid in period, we eventually found $P = 18.5611 \pm 0.0001$ hr, which seems to track certain features in the LP 12-502 light curve over its entire baseline.

What exactly is observed? For the first 64 cycles, the star shows a pattern reminiscent of an eclipsing binary, with four obvious local minima. We dub these dips $\{1,2,3,4\}$ at phases $\{-0.28,-0.08,0,0.25\}$, respectively. Over cycles 0 to 64, the depth of dips 1 and 3 remain roughly fixed. However dip 4 *decreases* in depth by about 2%, while dip 2 *increases* in depth, by about the same amount (see Figure 5). During cycles 48-64, it also seems that a fifth dip may be emerging, in the main "large" dip group.

There is then a 6-month (184 cycle) gap to Cycles 248-315, which show two intricately structured dip complexes, plus a small leading dip. The single leading dip is present at roughly the same phase as in cycles 0-64; they seem likely to be the same struture. Along a similar line of logic, it seems plausible that the first "dip complex" during cycles 248-264 represents an evolution of the initial complex seen during cycles 0-64, though with greatly reduced depth. During cycles 266-310, an additional local minimum develops between the two complexes; this feature is best visualized on the river plots (Appendix B), and we discuss its (shorter) period below.

The second dip complex during cycles 248-315 shows the most substructure. During e.g. cycles 283-298, this single complex shows six local minima. The deepest dip is sharp: it shows a flux exercusion of 3.5% over about 22 minutes ($0.02\,P$), which is the steepest slope exhibited anywhere in this object's remarkable dataset. After the sharp dip, there is a roughly exponential fall-off spanning about a quarter of a period, punctuated by coherent local minima and maxima which in detail (Appendix B) have slightly longer periods than the sharp dip. The sharp leading dip only decreases during a sudden state-switch at BTJD 2030.7 (cycles 299-315), which happens immediately during a flare (Figure 4). The trailing dips remain afterwards.

Sectors 53–58 (cycles 1233-1481) are comparitively tame; they showed only four to six dips per cycle. Some dips remain stable in depth and duration over this five month interval. Other dips grow, like the one at $\phi = +0.06$ between cycles 1499 and 1481. Other dips, such as the one at $\phi = +0.12$ in cycles 1233-1264, disappear entirely. The most dramatic state switch occurs during cycles 1233-1247, when a large dip "switches" from a depth of 3% and duration of 3 hours to a depth of 0.3%, and a duration of 1 hour.

4.2.2. *Lessons from LP 12-502*

STATE-SWITCHES REVEAL DIP INDEPENDENCE—The state-switches seen in cycles 1233-1247 and 299-315 confirm that dips can disappear in less than one cycle, a point which has been previously appreciated (Stauffer et al. 2017). What is new in these particular changes, for instance cycles 1233-1264 of Figure 5, is that the morphology changes show that the dips can be *independent* and *additive*. It other words, throughout cycles 1233-1264, there are three local minima between phases of 0 and 0.3. They all have identical ingress times. The shape change during the transition implies that the leading dip that "turned off" (changed its depth), while the trailing two dips remained fixed in their depths. In other words, the structures producing these dips must be independent, to the degree that one can undergo a severe change, while the others can remain essentially identical. The state switches during cycles 248-264 and 299-315 share the same characteristic: it is always the *leading* dip of a complex that "switches off", leaving the (fixed-depth) trailing dips in its wake.

SLOW GROWTH; RAPID DEATH—Although there are a few instances in which we observe dips "switch off" over less than one cycle, dip growth seems to happen more slowly. For instance, the dip that grows between phase 0 and 0.1 between cycles 260-290 begins to become visible around BTJD 1993.2, and growths in depth by about 2% over about six cycles, to become easily detectable by eye by BTJD 1997.7. The evolution of this particular dip is most clear in the river plots. The evolution of the latter dip group in cycles 1410-1481 is another example of this slow mode of dip growth.

DIP DURATIONS—The shortest timescale for any of the *individual* LP 12-502 dips seems to be $\approx 0.06\,P \approx 1.08$ hr. In comparison, using the stellar radius and mass derived in Section 2.3, the characteristic timescale $T_{\rm dur} \equiv R_\star P/(\pi a)$ for the transit of a point-source at corotation is 1.03 hr (**uncertainties?**). This means that while some of the LP 12-502 dips are sufficiently long to require structures that are extended in orbital azimuth, the durations of other dips are consistent with effective radii for the occulting material $R_{\rm eff} \ll R_\star$. This implies $a/R_\star \approx 5.8$ for this material, and so the analogous timescale at the stellar surface is about six times slower.

DIP PERIODS—Most of the LP 12-502 dips recur with a period of $P = 18.5611 \pm 0.0001$ hr. However the river plots (Appendix B) reveal multiple distinct periodicities in the light curve for specific dips. For instance, in sectors 25-26, the local minimum that develops around cycle 262 has a period faster than the mean period by $\approx$0.1%, while some of the trailing local minima in the main dip complex have periods slower than the mean period, by $\approx$0.04%. In addition to the fundamental period, we were able to identify at least four distinct periods shown by specific dips over the full Sectors 18-59 dataset, including periods at 18.5683, 18.5672, 18.5473, and 18.5145 hr, with a typical measurement uncertainty of $\approx$0.0002 hr. If each period corresponds to a dust clump, then this implies that multiple distinct clumps can orbit the star simultaneously, at marginally different separations.

5. DISCUSSION

5.1. *Extremes*

The closest CQV in our catalog is DG CVn (TIC 368129164; d=18 pc), a member of AB Dor. To our knowledge, this manuscript is the first time that it has been noted as a CQV. The three brightest CQVs are DG CVn (T=9.3), TIC 405754448 (T=9.6), and TIC 167664935 (T=10.3). The shortest period belongs to TIC 201789285, at 3.64 hr. The longest period belongs to TIC 405910546, at 37.9 hr. If the latter source turns out to be an eclipsing binary, the next-longest would be TIC 193831684 (31.0 hr).

The lowest mass ($\approx 0.12\,{\rm M}_\odot$) belongs to TIC 267953787. The catalog contains a few other stars with similar mass. Given the small number of sub-stellar mass objects in our target sample, this suggests that future studies of brown dwarf photometric variability might also yield complex quasiperiodic variables, though there would be degeneracies in interpretation with planetary surface features such as clouds and latitudinal bands (e.g. Apai et al. 2021; Vos et al. 2022).

The most massive CQV in our sample is a subject of some interest. To date, the only stars reported to show the CQV phenomenon are M-dwarfs, with typical stellar masses $\lesssim$0.3 ${\rm M}_\odot$ (Günther et al. 2022). TIC 405754448 and 405910546 however appear to have masses of 0.82 and 0.60 ${\rm M}_\odot$ respectively. The next-highest masses are $\approx$0.40 ${\rm M}_\odot$. The masses for the former two objects are consistent with their CAMD locations, and their membership in LCC. Based on its light curve morphology, TIC 405910546 should be studied in greater depth, to confirm it is not an eclipsing binary. TIC 405754448 similarly shows distinct morphology from many of the CQVs in Figure 2, in that it has some of the lowest amplitude dips. Nonetheless, both of these objects seem to suggest that the CQV phenomenon extends up in mass to pre-main-sequence K-dwarfs.

5.2. *CQVs are quasiperiodic*

A periodic signal repeats exactly; the CQVs do not (Figure 3). Their periods however do appear to be constant to within measurement precision over thousands of cycles. They are therefore *quasi*periodic. This point with previous studies by Günther et al. (2022) and Popinchalk et al. (2023). However it marks a qualitative departure from the "persistent" *vs.* "transient" flux dip distinction described by Stauffer et al. (2017); while the dips can persist over timescales of even up to 100 cycles, all CQV dips seem to be transient over timescales of more than 1000 cycles (Figure 3).

With that said, one might expect a truly quasiperiodic process to be able to explore all phase angles with equal weight. LP 12-502, and multiple other CQVs, seem to have preferred phases. For LP 12-502, all of the dips happen over phases corresponding to only two thirds of the period (Figure 5). The remaining third seems to be "out of limits" for any dipping material. This could be evidence that some aspect the stellar magnetic field is strongly asymmetric, and can generate and hold extrinsic material at corotation, but only over two thirds of the equatorial circle. Alternatively, the source of the material (e.g. a planetesimal swarm) might be distributed over an arc of the same angular extent (240°). We favor the former explanation, for reasons discussed below.

5.3. *Dip asymmetries and dust geometries*

The asymmetry of a dip can help diagnose the optical depth of the occulting material as a function of orbital phase angle. Sharp leading edges with trailing exponential egresses for instance have been previously seen for transiting exocomets and disintegrating rocky bodies (e.g. Rappaport et al. 2012; Brogi et al. 2012; Vanderburg et al. 2015; Zieba et al. 2019).

Examining Figure 2, it is not obvious whether the CQVs as a whole show any preference for sharper ingresses, or sharper egresses. In some cases (e.g. TIC 425933644), the continuum itself is not particularly well-defined, and so the meaning of "ingress" and "egress" are not particularly clear. In others, such as Sector 36 of TIC 89463560, there is a single clear sharp ingress with an exponential egress, which could be directly fit using e.g. a model analogous to those used for exocomets (e.g. Zieba et al. 2019). The main quantities of interest in such models would be the exponential decay time- and therefore length-scale, as well as the impact parameter and the inferred transit depth (and its implications for the equivalent "radius" of the transiting cloud). Although we briefly explored such models, it quickly became clear that careful modeling of sources such as LP 12-502 merits its own in-depth study. Connections could likely also be made to the toroidal geometries that are produced by outflowing atmospheres of transiting planets (e.g. McCann et al. 2019; MacLeod & Oklopčić 2022).

5.4. *Dust, or gas?*

We believe that the most likely scenarios to explain the overall CQV phenomenology are the dust clump scenario, or the prominence scenario (Figure 1). Both invoke clumpy material that would be centrifugally supported at the corotation radius. The prominence idea has a longer history, based first on analogy with quiescent prominences/filaments observed to exist in the solar corona for up to a few weeks (see e.g. 201 2015). In an extrasolar context, spectroscopic detections of transient Balmer- and resonance-line absorption seen for stars such as AB Dor and Speedy Mic (e.g. Collier Cameron & Robinson 1989; Jeffries 1993; Dunstone et al. 2006; Leitzinger et al. 2016) led to the interpretation that the data could best be explained by similar prominence structures: cold, minimally ionized hydrogen clouds or filaments that scatter chromospheric emission from the star to produce the observed spectroscopic line variations (see Collier Cameron & Robinson 1989). The (short-term) mechanical stability of such gas configurations has been demonstrated (Ferreira 2000; Waugh & Jardine 2022), and the interpretation of this class of observations seems at least somewhat secure.

The link between the dense gas clumps (prominences) that likely exist around rapidly rotating low-mass stars, and the CQV phenomenon, has yet to be made. A simple visual examination of the TESS light curves for five prominence-hosting systems studied by Jardine & Collier Cameron (2019)–AB Dor, Speedy Mic, LQ Lup, HK Aqr, and V374 Peg–revealed no obvious CQV behavior, though all likely show differential rotation, and Speedy Mic shows two closely-spaced periods and a strong beat. Spectroscopically observable prominences therefore do not imply CQV-like dips.

The difference between the prominence and dust clump scenarios is essentially only in whether the occulting material of interest is neutral hydrogen, or dust. In the phrasing of the "frozen flux" condition of ideal rigid field magnetohydrodynamics, the tendency of both to become trapped at the corotation radius in the equatorial plane is tied to how of the four relevant forces (gravity, Lorentz, inertial Coriolis, and inertial centrifugal), the Lorentz and Coriolis only act perpendicular to field lines, while gravity and the centrifugal force are in balance at $R_{\rm cr}$ (see Townsend & Owocki 2005, Sec. 2). The magnetic field strength is only relevant in this formulation of the system in that we must have $R_{\rm sonic} < R_{\rm cr} < R_{\rm Alfven}$ in order for closed loops to exist that can support prominences (Jardine & Collier Cameron 2019) **lgb todo: verify & dejargonify!**. In detail however, whether such magnetic fixed points lie in the equatorial plane, or elsewhere, depends on the star's magnetic field geometry (Sanderson et al. 2023).

5.4.1. *Can gas absorption reproduce the observed chromaticity?*

The strongest argument for why neutral hydrogen is an unlikely occulting source is that CQVs show broadband flux variations that are deeper in the blue than in the red.

Based on our reading of Gray (1992, Ch. 8), it seems somewhat challenging to get neutral hydrogen to have this type of chromaticity. Bound-bound absorption provides opacity only at narrow resonant lines. Bound-free absorption can provide wavelength-dependent opacity, but the absorption coefficients generally *grow* with increasing wavelength, rather than *shrink* as one needs in order to get deeper absorption in the blue than in the red. H^- fails as a viable opacity source for the same reason: its absorption coefficient peaks near 8500 Å, and is an order of magnitude smaller at ≈3000Å. (Gray 1992), following Wishart (1979). Thompson scattering is also ruled out, because it is gray. Dust, with its relatively featureless but increasing extinction curve when going bluer into the optical (Cardelli et al. 1989), is to our knowledge the most obvious opacity source.

While the above line of reasoning seems fairly convincing, it has a flaw. The logic presented above would imply that regardless of a star's temperature, if relative depths of a dip are seen to be deeper in the blue than in the red, then it is hard to get hydrogen to do it. There is however a rapidly rotating magnetic B-star, σ Ori E, which shows dips that are deeper in the blue than in the red (Hesser et al. 1977). Photometric and spectroscopic observations of this star have been understood in terms of absorbing circumstellar material, quite analogous to the geometries we are discussing for much cooler M-dwarfs (Townsend et al. 2005). This material however cannot be dust, due to the relevant sublimation timescales. It is instead thought to be sourced from bound-free absorption from neutral hydrogen (Townsend et al. 2005). Separate and smaller amplitude emission in that system may also come from electrons scattering photospheric light toward the observer when the clouds are not in transit (Berry et al. 2022).

Given these complexities, it clearly seems important for a future theoretical study to be conducted to determine to what degree the observed chromaticities in CQVs match, or do not match, expectations from radiative transfer. This issue has a key ability to resolve the question of whether the CQVs are caused by dust, or by gas. This question has direct bearing on the potential utility of these objects.

5.5. *Planets or planetesimal swarms near corotation?*

Planet occurrence rate studies based on Kepler showed that around (early) M-dwarfs, there are $\approx$0.1 planets per star with sizes between 1-4 $R_\oplus$ and orbital periods within 3 days (Dressing & Charbonneau 2015). The number increases to $\approx$0.7 planets per star, for planets with 1-4 $R_\oplus$ and $P<10$ days. Extrapolating to all small close-in planets, from say 0.1-4 $R_\oplus$ and within 10 days, it is reasonable to expect on average one planet per M-dwarf. TRAPPIST-1b (P=1.5 days) is one example of this type of planet, in orbit around a 0.08 $M_\odot$ star (Gillon et al. 2017).

In the context of planet formation theory, the locations of these close-in planets are set by the location of the protoplanetary disk's magnetospheric truncation radius (see e.g. CITE for a review). In simple 1-D viscous accretion models, this truncation radius roughly coincides with the corotation radius (CITE), though in detail factors of a few difference have been observed between the two (CITE IR studies). Within models that have migrating compact multiplanet resonant chains, the inner-most planets arrive within $\approx$5-10 stellar radii within the first 100 Myr (Izidoro & Raymond 2018).

It is tempting to try to interpret features of the CQV light curves in terms of the possible presence of close-in exoplanets, or even planetesimals. Rocky planets this young would likely have molten global magma oceans analogous to those that existed on the Earth and Moon (see Lichtenberg et al. 2022), and thus would being undergoing significant outgassing and atmospheric escape. While a scenario in which close-in rocky planets serve as a possible source of dust for the clouds is *a priori* plausible, it is currently only a subject of speculation.

Given the dip depth variations that are observed in systems like LP 12-502, one might be driven in this framework toward a picture of a disintegrating planetesimal swarm. The sizes of the planetesimals would need to be $\lesssim 1\,R_\oplus$, based on the non-detections of their transits, analogous to e.g. K2-22 (Sanchis-Ojeda et al. 2015) or KOI-2700 (Rappaport et al. 2014). The dip-profile asymmetries during certain segments of the light curve plausibly match this idea; for instance, the complex in cycles 248-298 could be well-fit by a sharp leading edge that decays over 0.2 P (3.7 hours). The earlier complex, during cycles 248-264 (pre-state-switch), could be fit by a similar profile. While the number of free parameters in this type of model is somewhat dizzying, we have no right to believe that nature need be simple.

Ultimately, there are a few problems for the idea of a disintegrating planetesimal. First, a large number of the dips show asymmetries in the *wrong direction* relative to the naive expectation of a trailing comet tail. Invoking non-exponentially decaying dust distributions as a function of azimuth might be one way out of this, but such an idea would need stronger theoretical footing. More important is that the (unseen) planets or planetesimals should be on *exactly periodic* orbits over observable timescales, on the presumption that the planetesimals would be massive enough to not feel any headwind or magnetic field. For most CQVs, this is inconsistent with the data; dips in sources such as LP 12-502 appear and disappear at *distinct phases*, but with the same period. It seems challenging to reconcile this behavior with the possible presence of just a single launching body. Finally, the fact that the dips often respond to events like flares suggests that that the responsible material be much less massive than a 1–100- km sized planetesimal, and therefore more easily influenced by the stellar magnetic field.

It is certainly possible that exoplanets could end up being connected to the CQV phenomenon, for instance as a possible source of dust through collisions at greater separations from the star. However for the time being, none of the CQVs that we have studied in this work seem to show clear evidence for an exoplanetary origin.

5.6. *From dippers to debris disks*

It is amusing that in identifying the two candidate CQV sources in Section 3.3 with outlying SEDs (TICs 193136669 and TIC 57830249), we were prompted to reconsider our labelling, to ultimately conclude that these sources are dippers. This episode suggeests that could be some overlap between the two classes of object. It is also worth emphasizing that our labelling of e.g. TIC 57830249 was based on a single sector of TESS data (Sector 36) when its behavior is relatively periodic and it showed relative dip depths of a few percent. However in other TESS sectors (e.g. Sector 10), this source looks completely different, varying in apparent flux by a factor of two, with hardly any discernable periodicity at all.

Comparing these results against the backdrop of our increasing understanding of dippers (e.g. Cody et al. 2014; Ansdell et al. 2016; Robinson et al. 2021; Capistrant et al. 2022), it is clear that the loss of an infrared excess is associated with strong changes in a star's optical variability. It is reasonable to imagine connections between CQVs and dippers: both classes of object can show transient flux dips that are relatively narrow in duration. Such dips in both are probably associated with clumps of dust or gas. However the CQV dips are typically *i)* more periodic and *ii)* less deep than those of dippers, and *iii*) they display far less transience over timescales of a few to tens of cycles. This is probably because CQV stars have demonstrably less dust than (most) dipper stars. At a population level, the CQV stars are also older. A common mystery between the CQVs and dippers, in our own estimation, is how exactly the *narrowness* of the dust clumps is produced. It is not unreasonable to imagine a similar mechanism operating for both types of object, tied perhaps to a shared magnetic topology, or perhaps to a preference for dust to inspiral to the star in clumped structures.

5.7. *Are half-cycles important?*

The interval of half a cycle period could be significant in the context of CQVs for two reasons. The first is that for material on a circular orbit viewed edge-on, it corresponds to the interval between transit and secondary eclipse. The second is that it also corresponds to the interval over which half of the star's surface is visible. Of the CQVs in Figures 2 and 3, a number that seems greater than random might exhibit a preference for showing dips or peaks that correspond to the half-cycle interval.

One set of CQVs shows "CQV behavior" (some form of dip complex), but which only lasts for half of any given cycle. TIC 206544316 (Sector 2) is a canonical example; TIC 405910546 (Sector 38), TIC 167664935 (Sector 38), TIC 146539195 (Sector 5), TIC 118449916 (Sector 44), and TIC 312410638 (Sector 38) seem to show essentially the same tendency.

An independent set of CQVs exhibits small dips roughly half a cycle after large dips; it is tempting to label the small dips secondary eclipses. Such sources include TIC 402980664 (Sector 25; relative to the sharpest, deepest minimum), TIC 89463560 (Sector 36), TIC 224283342 (Sector 2), and TIC 442571495 (Sector 12).

It is challenging to interpret the significance of such apparent regularities; the objects exhibit such a wide range of variability that for seemingly any "regularity" one might posit, it is easy to come up with counter-example objects which do not follow the trend. In other words, these half-cycle CQVs could simply be a product of the human tendency to pattern match; alternatively, they might yield some important physical signifiance.

5.8. *Mass flux estimate*

We can estimate the mass of a transiting cloud by first converting the transit depth to an effective cloud radius, $R_{\rm cloud}$. For most CQVs in Figure 2, this typically yields $\approx$2-20 $R_\oplus$. This size can be converted into a mass estimate by requiring the optical depth τ of the cloud to be at least unity and by positing some composition for the cloud. In other words, a minimum constraint on the number density follows by requiring the cloud to be optically thick. For cases like LP 12-502, this is resonable because the transit duration implies $R_{\rm cloud} \ll R_\star$. Carrying out the relevant calculation assuming a dust composition, for dust grains 1 μm in size, Sanderson et al. (2023) find minimum cloud masses of order 10^{12} kg (their Eq. 23), which scale linearly with both the optical depth and dust grain radius. This is roughly comparable to a small asteroid; the asteroid belt itself has a mass of order $\approx 10^{21}$ kg (CITE). Also by way of comparison, the previously-discussed cool gas prominences for AB Dor would need to have masses of order 10^{14} kg (Collier Cameron et al. 1990), about 100$\times$ larger than the requisite dust mass.

Our observations provide a direct measurement of how often dips appear and disappear, both due to sudden state-switches, and due to more gradual, secular evolution. For instance, LP 12-502 showed three "state-switch" events over the six months of available TESS observations, during cycles 248-264, 299-315, and 1233-1247. It is plausible to imagine that these events correspond to either mass being ejected from corotation, or perhaps being accreted onto the star. In either case, the corresponding $\dot{M} \equiv M \cdot {\rm d}N/{\rm d}t$ is $\approx 3\times 10^{-18} M_\odot\,{\rm yr}^{-1} \approx 1\times 10^{-12} M_\oplus\,{\rm yr}^{-1}$. Considered cumulatively over the $\approx 10^8$ years for which the CQV phenomenon is observed, this yields a cumulative moved dust mass of $10^{-4} M_\oplus$, of order the Solar System's asteroid belt. If the occulting material is gas, the masses involved would be of order 100 times larger.

6. CONCLUSIONS

In this work, we analyzed TESS 120-second cadence data collected between July 2018 and Sep 2022, and searched it for complex quasiperiodic variables (CQVs). Our search sample included 65,760 K- and M-dwarfs within 150 pc, and was $\gtrsim 80\%$ complete within 30 pc, and $\lesssim 10\%$ complete at distances exceeding 100 pc.

In this sample of stars, we found 53 objects that showed complex quasiperiodic behavior over at least one TESS sector. Because the TESS 120-second stellar sample was rooted in a heterogeneous selection function that may have been biased in favor of young stars over field stars, we caution against interpreting our detection statistics in terms of broader population occurrence rates. The 53 bonafide CQVs are listed in Table **??**. This table also includes an additional 17 candidate CQVs, whose designation is less certain.

Analyzing the CQV light curves, we draw the following conclusions.

- CQVs are *quasi*periodic. While the mean periods in our sample seem to remain fixed over the span of available observations, the light curve shapes themselves evolve, similar to rotating stars.
- The same CQV can show dips with similar but clearly distinct periods. LP 12-502, for instance, showed dips with four distinct periods within $\pm 0.3\%$ of its fundamental period, sometimes simultaneously, and each lasting for up to 50 cycles.
- The CQV phenomenon persists for at least 150 Myr, based on the existence of multiple CQVs in AB Dor, the Pleiades, and Psc-Eri. It may extend to even older ages, however the lack of detected CQVs in the Hyades and Praesepe suggests that the phenomenon does become less common at older ages.
- CQVs evolve over timescales that are both secular (>100 cycles) and impulsive (<1 cycle). "State-

switches" can cause dips to collapse instantaneously, and are often (but not exclusively) linked with observed optical flares. Dip growth however seems to happen over durations of at least ten cycles, and slow dip decay also happens.

- The duty cycle for CQVs seems to be $\approx 75\%$, based on the fraction of bonafide CQVs that turned on or turned off during TESS re-observations, two years after their initial observation.

Many questions remain. Is the eclipsing material responsible for the phenomenon gas, or dust? After correcting for line-of-sight inclination, do most M-dwarfs go through a phase of trapping material a few stellar radii away from their surfaces? What observational signatures distinguish the proposed models (Figure 1, bottom row)? What organizational regularities characterize the CQV as a class of variable star? What physically sets the extremes of the CQV population, such as the longest rotation periods, hottest stellar temperatures, and oldest stellar ages? And finally, what connections, if any, do CQVs have to topics such as stellar evolution, M-dwarf magnetic fields, debris disks, and close-in exoplanets? While we have tried to point out possible connections, the most likely path toward definitive resolutions would be to observe a full phase curve of LP 12-502, or perhaps some other suitable object, using JWST/MIRI.

lgb: final paragraph(s) clearly need improvement!

ACKNOWLEDGMENTS

This work was supported by the Heising-Simons 51 Pegasi b Fellowship (LGB). TIC 402980664 was observed at 120-second cadence thanks to the TESS Guest Investigator programs G022252 (PI: J. Schlieder; Sectors 18, 19, 25, 26) and G04168 (PI: R. Jayaraman; Sector 53).

DRAFT AUTHOR CONTRIBUTION STATEMENTS – PLEASE REVISE IF APPROPRIATE) LGB and RJ conceived the project and executed the dip-based and Fourier-based searches, respectively. LGB drafted the initial manuscript, and performed the cluster membership, SED, and variability analyses. SR and RJ vetted the results from the Fourier search. LAH advised on project scope and experiment design. GAB acquired and maintained the servers used to run the dip-finding pipeline. GRR is an architect of the TESS mission, and advised RJ on his contributions. All authors assisted in manuscript revision.

Software: `astrobase` (Bhatti et al. 2021), `lightkurve` (Lightkurve Collaboration et al. 2018), `scipy` (Virtanen et al. 2020), `TESS-point` (Burke et al. 2020),

Facilities: *Astrometry*: Gaia (Gaia Collaboration et al. 2018, 2022). *Imaging*: Second Generation Digitized Sky Survey. *Spectroscopy*: Keck:I (HIRES; Vogt et al. 1994). *Photometry*: TESS (Ricker et al. 2015), *Broadband photometry*: 2MASS (Skrutskie et al. 2006), APASS (Henden et al. 2016), Gaia (Gaia Collaboration et al. 2018,?), SDSS (York et al. 2000), WISE (Wright et al. 2010).

REFERENCES

2015, Astrophysics and Space Science Library, Vol. 415, Solar Prominences

Allard, F., Homeier, D., & Freytag, B. 2012, Philosophical Transactions of the Royal Society A: Mathematical, Physical and Engineering Sciences, 370, 2765

Ansdell, M., Gaidos, E., Rappaport, S. A., et al. 2016, ApJ, 816, 69

Apai, D., Nardiello, D., & Bedin, L. R. 2021, ApJ, 906, 64

Asplund, M., Grevesse, N., Sauval, A. J., & Scott, P. 2009, ARA&A, 47, 481

Bailer-Jones, C. A. L., Rybizki, J., Fouesneau, M., Demleitner, M., & Andrae, R. 2021, AJ, 161, 147

Barber, R. J., Tennyson, J., Harris, G. J., & Tolchenov, R. N. 2006, MNRAS, 368, 1087

Basri, G. 2021, An Introduction to Stellar Magnetic Activity

Bell, C. P. M., Mamajek, E. E., & Naylor, T. 2015, MNRAS, 454, 593

Berry, I. D., Owocki, S. P., Shultz, M. E., & ud-Doula, A. 2022, MNRAS, 511, 4815

Bhatti, W., Bouma, L., Joshua, et al. 2021, waqasbhatti/astrobase: astrobase v0.5.3, Zenodo

Bodman, E. H. L., Quillen, A. C., Ansdell, M., et al. 2017, MNRAS, 470, 202

Bouma, L. G., Winn, J. N., Ricker, G. R., et al. 2020, AJ, 160, 86

Bouma, L. G., Curtis, J. L., Masuda, K., et al. 2022, AJ, 163, 121

Boyle, A. W., & Bouma, L. G. 2023, AJ, 166, 14

Bressan, A., Marigo, P., Girardi, L., et al. 2012, MNRAS, 427, 127

Brogi, M., Keller, C. U., de Juan Ovelar, M., et al. 2012, A&A, 545, L5

Burke, C. J., Levine, A., Fausnaugh, M., et al. 2020, TESS-Point: High precision TESS pointing tool, Astrophysics Source Code Library, record ascl:2003.001

Cantat-Gaudin, T., Anders, F., Castro-Ginard, A., et al. 2020, A&A, 640, A1

Capistrant, B. K., Soares-Furtado, M., Vanderburg, A., et al. 2022, ApJS, 263, 14

Cardelli, J. A., Clayton, G. C., & Mathis, J. S. 1989, ApJ, 345, 245

Chen, Y., Girardi, L., Bressan, A., et al. 2014, MNRAS, 444, 2525

Cody, A. M., Stauffer, J., Baglin, A., et al. 2014, AJ, 147, 82

Collier Cameron, A. 1999, in Astronomical Society of the Pacific Conference Series, Vol. 158, Solar and Stellar Activity: Similarities and Differences, ed. C. J. Butler & J. G. Doyle, 146

Collier Cameron, A., Duncan, D. K., Ehrenfreund, P., et al. 1990, MNRAS, 247, 415
Collier Cameron, A., & Robinson, R. D. 1989, MNRAS, 238, 657
Dahm, S. E. 2015, ApJ, 813, 108
David, T. J., & Hillenbrand, L. A. 2015, ApJ, 804, 146
Dressing, C. D., & Charbonneau, D. 2015, ApJ, 807, 45
Dunstone, N. J., Barnes, J. R., Collier Cameron, A., & Jardine, M. 2006, MNRAS, 365, 530
Fausnaugh, M., Morgan, E., Vanderspek, R., et al. 2021, PASP, 133, 095002
Feiden, G. A. 2016, A&A, 593, A99
Ferreira, J. M. 2000, MNRAS, 316, 647
Gagné, J., Mamajek, E. E., Malo, L., et al. 2018, ApJ, 856, 23
Gaia Collaboration, Brown, A. G. A., Vallenari, A., et al. 2018, A&A, 616, A1
Gaia Collaboration, Vallenari, A., Brown, A. G. A., et al. 2022, arXiv e-prints, arXiv:2208.00211
Gillon, M., Triaud, A. H. M. J., Demory, B.-O., et al. 2017, Nature, 542, 456
Gray, D. F. 1992, The observation and analysis of stellar photospheres., Vol. 20
Gully-Santiago, M. A., Herczeg, G. J., Czekala, I., et al. 2017, ApJ, 836, 200
Günther, M. N., Berardo, D. A., Ducrot, E., et al. 2022, AJ, 163, 144
Henden, A. A., Templeton, M., Terrell, D., et al. 2016, VizieR Online Data Catalog, II/336
Hesser, J. E., Ugarte, P. P., & Moreno, H. 1977, ApJL, 216, L31
Hippke, M., David, T. J., Mulders, G. D., & Heller, R. 2019, AJ, 158, 143
Izidoro, A., & Raymond, S. N. 2018, in Handbook of Exoplanets, ed. H. J. Deeg & J. A. Belmonte, 142
Jardine, M., & Collier Cameron, A. 2019, MNRAS, 482, 2853
Jeffries, R. D. 1993, MNRAS, 262, 369
Jenkins, J. M., Twicken, J. D., McCauliff, S., et al. 2016, in Society of Photo-Optical Instrumentation Engineers (SPIE) Conference Series, Vol. 9913, Software and Cyberinfrastructure for Astronomy IV, ed. G. Chiozzi & J. C. Guzman, 99133E
Justesen, A. B., & Albrecht, S. 2021, ApJ, 912, 123
Kerr, R. M. P., Rizzuto, A. C., Kraus, A. L., & Offner, S. S. R. 2021, ApJ, 917, 23
Koen, C. 2021, MNRAS, 500, 1366
—. 2023, MNRAS, 518, 2921
Leitzinger, M., Odert, P., Zaqarashvili, T. V., et al. 2016, MNRAS, 463, 965
Lichtenberg, T., Schaefer, L. K., Nakajima, M., & Fischer, R. A. 2022, arXiv e-prints, arXiv:2203.10023
Lightkurve Collaboration, Cardoso, J. V. d. M., Hedges, C., et al. 2018, Lightkurve: Kepler and TESS time series analysis in Python, Astrophysics Source Code Library, record ascl:1812.013
MacLeod, M., & Oklopčić, A. 2022, ApJ, 926, 226
McCann, J., Murray-Clay, R. A., Kratter, K., & Krumholz, M. R. 2019, ApJ, 873, 89
Meingast, S., Alves, J., & Rottensteiner, A. 2021, A&A, 645, A84
Onitsuka, M., Fukui, A., Narita, N., et al. 2017, PASJ, 69, L2
Palumbo, E. K., Montet, B. T., Feinstein, A. D., et al. 2022, ApJ, 925, 75
Pecaut, M. J., & Mamajek, E. E. 2013, ApJS, 208, 9
Popinchalk, M., Faherty, J. K., Curtis, J. L., et al. 2023, ApJ, 945, 114
Rajpurohit, A. S., Reylé, C., Allard, F., et al. 2013, A&A, 556, A15
Rappaport, S., Barclay, T., DeVore, J., et al. 2014, ApJ, 784, 40
Rappaport, S., Levine, A., Chiang, E., et al. 2012, ApJ, 752, 1
Ratzenböck, S., Meingast, S., Alves, J., Möller, T., & Bomze, I. 2020, A&A, 639, A64
Rebull, L. M., Stauffer, J. R., Cody, A. M., et al. 2018, AJ, 155, 196
Rebull, L. M., Stauffer, J. R., Bouvier, J., et al. 2016, AJ, 152, 114
Ricker, G. R., Winn, J. N., Vanderspek, R., et al. 2015, Journal of Astronomical Telescopes, Instruments, and Systems, 1, 014003
Robinson, C. E., Espaillat, C. C., & Owen, J. E. 2021, ApJ, 908, 16
Rodriguez, D. R., van der Plas, G., Kastner, J. H., et al. 2015, A&A, 582, L5
Sanchis-Ojeda, R., Rappaport, S., Pallè, E., et al. 2015, ApJ, 812, 112
Sanderson, H., Jardine, M., Collier Cameron, A., Morin, J., & Donati, J. F. 2023, MNRAS, 518, 4734
Skrutskie, M. F., Cutri, R. M., Stiening, R., et al. 2006, AJ, 131, 1163
Somers, G., Cao, L., & Pinsonneault, M. H. 2020, ApJ, 891, 29
Speagle, J. S. 2020, MNRAS, 493, 3132
Stassun, K. G., Kratter, K. M., Scholz, A., & Dupuy, T. J. 2012, ApJ, 756, 47
Stassun, K. G., Oelkers, R. J., Pepper, J., et al. 2018, AJ, 156, 102
Stauffer, J., Collier Cameron, A., Jardine, M., et al. 2017, AJ, 153, 152
Stauffer, J., Rebull, L., David, T. J., et al. 2018, AJ, 155, 63
Stellingwerf, R. F. 1978, ApJ, 224, 953
Tanimoto, Y., Yamashita, T., Ui, T., et al. 2020, PASJ, 72, 23
Townsend, R. H. D., & Owocki, S. P. 2005, MNRAS, 357, 251
Townsend, R. H. D., Owocki, S. P., & Groote, D. 2005, ApJL, 630, L81
Vanderburg, A., Johnson, J. A., Rappaport, S., et al. 2015, Nature, 526, 546
Vines, J. I., & Jenkins, J. S. 2022, MNRAS, 513, 2719
Virtanen, P., Gommers, R., Oliphant, T. E., et al. 2020, Nature Methods, 17, 261

Vogt, S. S., Allen, S. L., Bigelow, B. C., et al. 1994, in Society of Photo-Optical Instrumentation Engineers (SPIE) Conference Series, Vol. 2198, Instrumentation in Astronomy VIII, ed. D. L. Crawford & E. R. Craine, 362

Vos, J. M., Faherty, J. K., Gagné, J., et al. 2022, ApJ, 924, 68

Waugh, R. F. P., & Jardine, M. M. 2022, MNRAS, 514, 5465

Winn, J. N. 2010, in Exoplanets, ed. S. Seager, 55

Wishart, A. W. 1979, MNRAS, 187, 59P

Wright, E. L., Eisenhardt, P. R. M., Mainzer, A. K., et al. 2010, AJ, 140, 1868

York, D. G., Adelman, J., Anderson, John E., J., et al. 2000, AJ, 120, 1579

Zhan, Z., Günther, M. N., Rappaport, S., et al. 2019, ApJ, 876, 127

Zieba, S., Zwintz, K., Kenworthy, M. A., & Kennedy, G. M. 2019, A&A, 625, L13

Zuckerman, B. 2019, ApJ, 870, 27

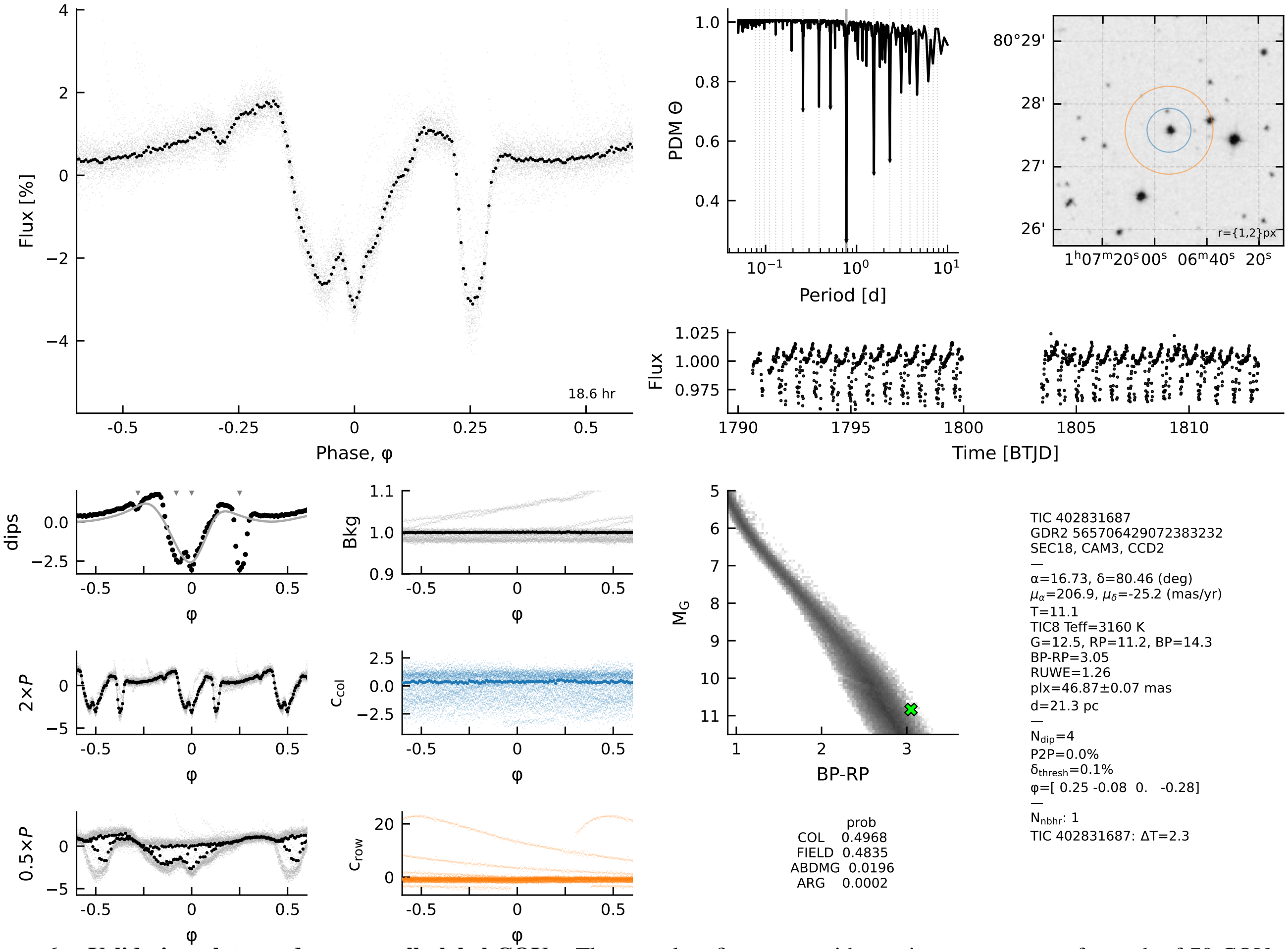

Figure 6. **Validation plots used to manually label CQVs**. The complete figure set, with one image per sector for each of 70 CQVs and candidate CQVs is available online **For internal collaboration review: https://www.dropbox.com/scl/fo/zlj3txot4cvymfb22wewu/h?dl=0&rlkey=3ec5f9o5xewrixzfkhkdenopa**. Panels are as follows. *a)*: Phase-folded light curve; gray points are raw 2-minute data and black points are binned to 200 points per cycle. *b)*: Phase-dispersion minimization (PDM) periodogram. Dotted lines show up to the 10^{th} harmonic and subharmonic. *c)*: DSS finder chart, with 1- and 2-TESS pixel radius circles displayed for scale. *d)*: Cleaned light curve, binned to 20-minute cadence, in Barycentric TESS Julian Date (BTJD). *e)*: Phase-folded light curve, binned to 100 points per cycle. The gray line denotes the automated spline-fit to the wrapped phase-folded light curve, and small gray triangles denote automatically identified local minima. *f)*: Phase-folded light curve at twice the peak period. *g)*: Phase-folded light curve at half the peak period. *h)*: Phase-folded time-series within the "background" aperture defined in the SPOC light curves. *i)*: Phase-folded flux-weighted centroid in the column direction. *j)*: Phase-folded flux-weighted centroid in the row direction. *k)*: Gaia DR2 color–absolute magnitude diagram. The gray background denotes stars within 100 pc. *l)*: Information from Gaia DR2, TIC8, and the automated dip-counting search pipeline. "Neighbors", abbreviated "nbhr", are listed within apparent distances of 2 TESS pixels if $\Delta T < 2.5$. *m)*: BANYAN-Σ v1.2 association probabilities, calculated using positions, proper motions, and the parallax.

APPENDIX

A. VALIDATION PLOTS

Figure 6 shows the type of plot used to visually assess whether a source was likely to be a CQV, eclipsing binary, or simply a rapidly rotating star.

B. LP 12-502

The light curve— Figure 7 shows another alternative view of Figure 5, but arranged to enable easy visual appreciation of transit timing changes, rather than transit depth changes. A best-fitting two-harmonic sinusoid has been independently fitted and subtracted from the Sector 18-19 data, 25-26 data, and 53, 58, and 59 data.

Finally, Figure 8 shows "river plots" of the same data, split into similar intervals: the Sector 18-19 data, 25-26 data, 53 data, and 58-59 data. State changes are evident in these plots whenever there is a sudden change in color. **todo: fix missing data to be different from the flare color**

C. MORE NEAT PLOTS

Figures 9 and 10 show 120-second cadence data for TIC 300651846, a CQV in the TESS continuous viewing zone. With the exception of a few sectors, TESS data will exist for this source over Sectors 1-12, 27-39, and 61-69. The majority are in the full frame images, and are the subject of future work.

D. NO ADDITIONAL POWER AT 20 SECOND CADENCE

Going from K2 to TESS, an important discovery was that the CQV shapes can significantly evolve, since the stars can vary over timescales of just a few minutes. We observed a set of CQVs between 2020 and 2021 using the TESS 20-second cadence mode (TESS DDT029). **todo: list the stars. todo: examine the 2min vs 20sec periodograms, and summarize in a few sentences whether any difference is there.**

E. CHROMATICITY IN TIC 262400835

TIC 262400835 (d=174 pc) is formally outside the scope of the current work. However, this CQV was observed using MuSCAT2 on 2020 December 12, 13, and 16, and the results are pertinent enough to the present work. **todo: describe observations**.

We include **a table of the photometry** here to enable potential future deeper analyses of the chromaticity of this object class.

Generally, these data serve as a minor addition beyond the observations that have been acquired by Onitsuka et al. (e.g. 2017); Tanimoto et al. (e.g. 2020); Günther et al. (e.g. 2022); Koen (e.g. 2023) on this topic. Koen (2023) provides what we find to be the most lucid summary, and we quote: "amplitudes are almost always larger, the shorter the wavelength of the filter, but the relationship can be weak or non-monotonic."

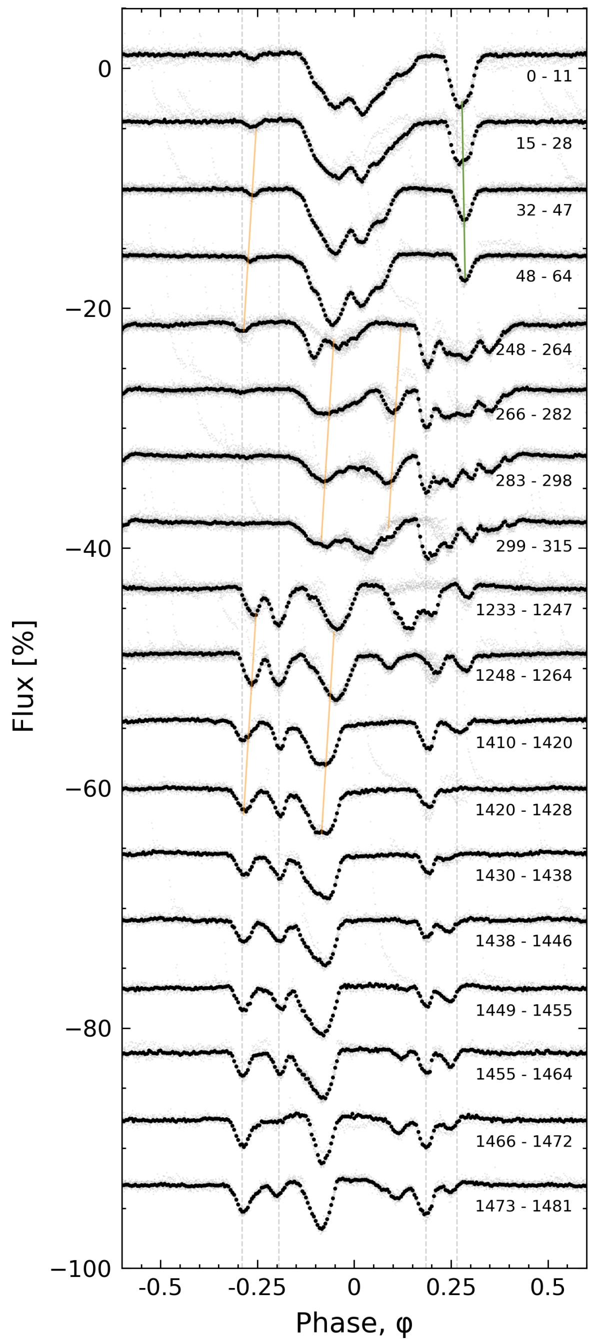

Figure 7. Alternative view of the evolution of LP 12-502 (Figure 5), arranged to emphasize changes in transit times. There are 200 binned black points per cycle; a two-harmonic sinusoid has been subtracted over specific chunks in time (**see text**). Vertical gray lines are underplotted to help guide the eye to instances in which preferred dip phases synchronize over long baselines. The orange and green lines guide the eye to where dips appear to change the positions of their local minima.

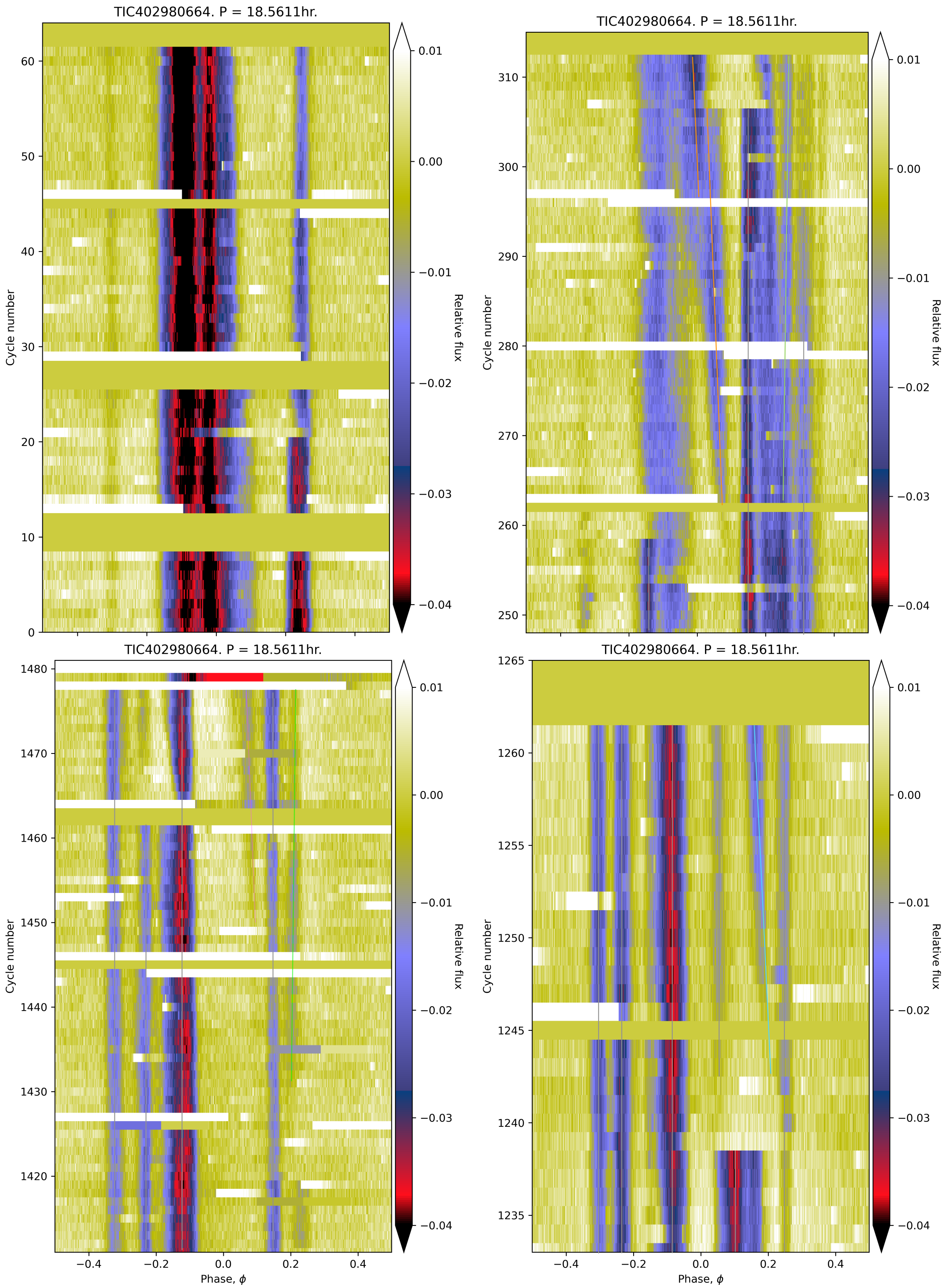

Figure 8. River plots of LP 12-502, showing (clockwise from top-left) Sectors 18-19, 25-26, 53, and 58-59. A two-harmonic sinusoid has been subtracted over specific chunks in time (**see text**). For Sectors 25-26 (cycles 248-315), three periods are overplotted: P=18.5611 hr (gray vertical line); 18.5404 hr (orange); 18.5683 hr (green). For Sector 53, gray is identical, while cyan is 18.5145 hr. For Sectors 58-59, the magenta line is 18.5473 hr, and the green line is 18.5672 hr.

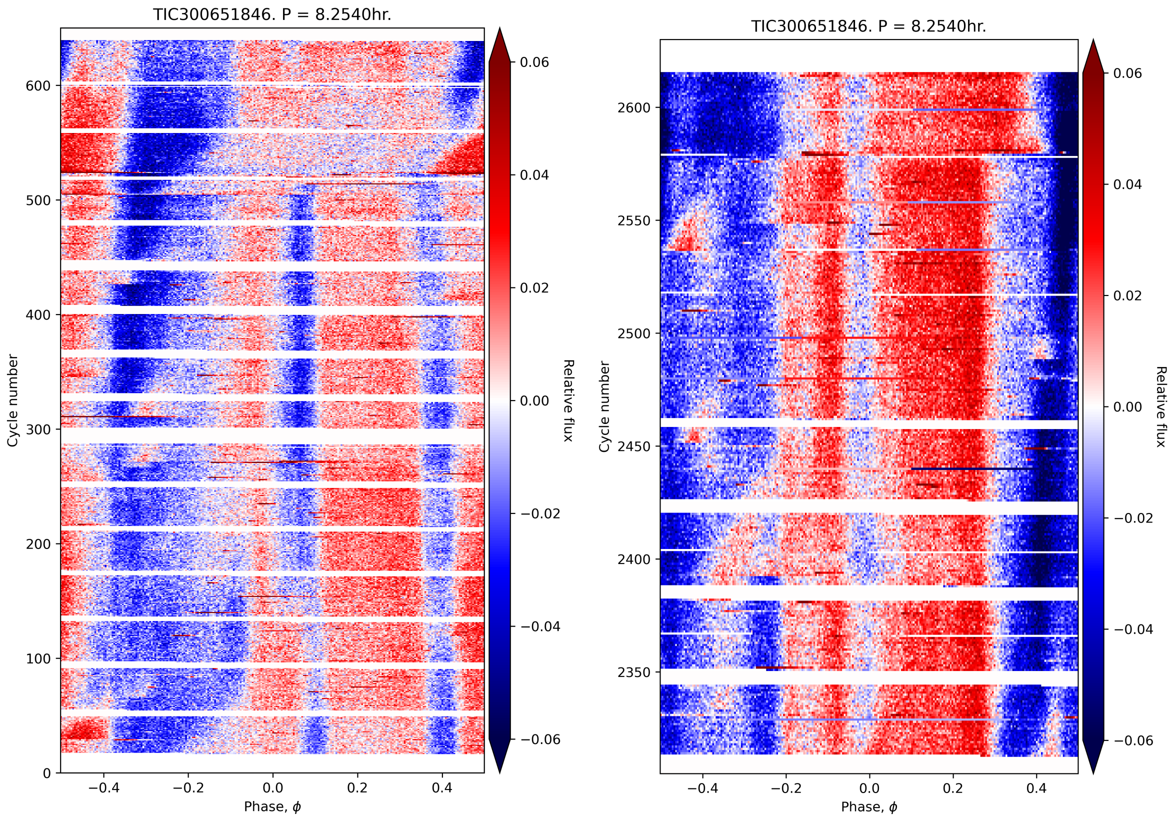

Figure 9. River plots of TIC 300651846. The envelope has not been subtracted. 7 sectors of continuous 2-minute observations S32-S39. (Thanks to DDT029) Then a few in S60+ on the right. Compare to Figure 2.

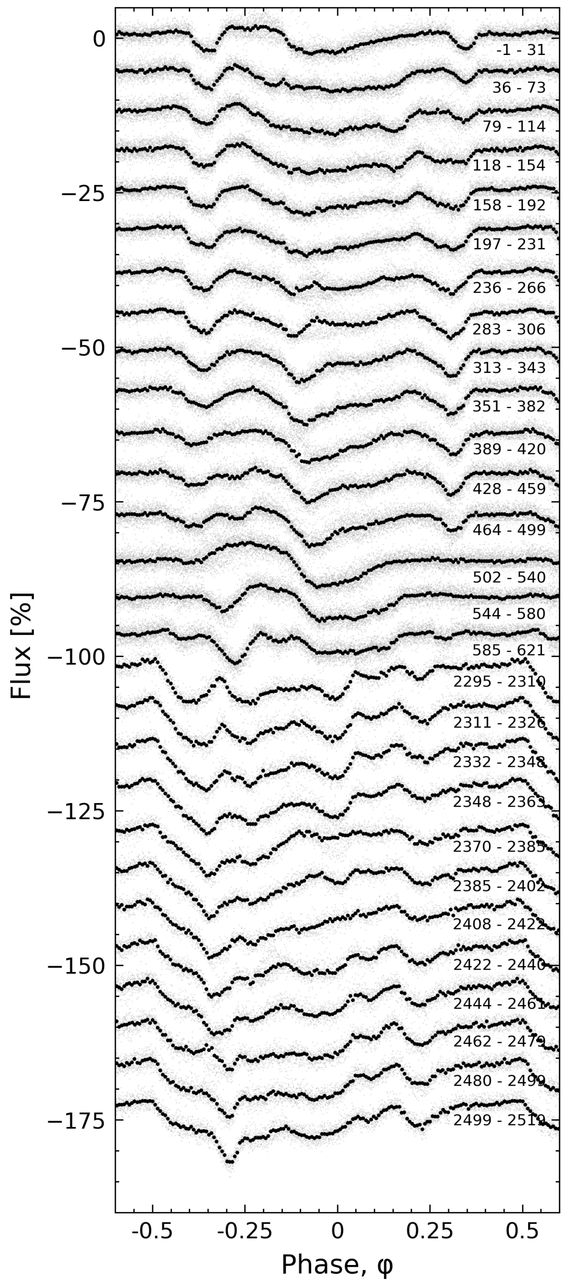

Figure 10. Orbit-phased plots of TIC 300651846. The envelope has not been subtracted.

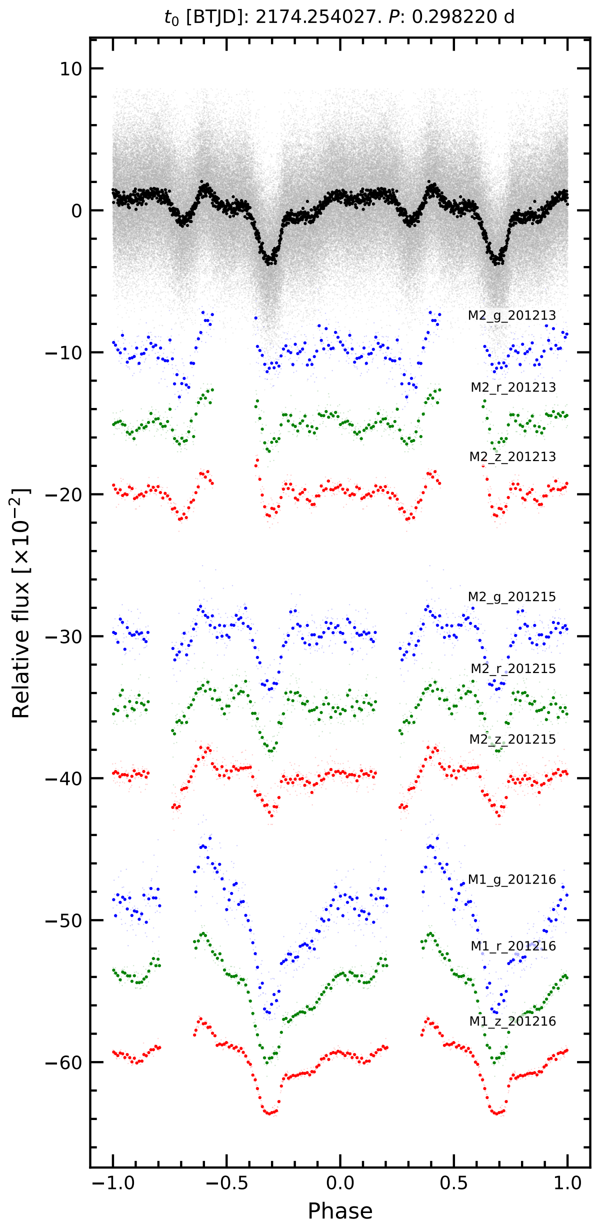

Figure 11. Chromaticity in TIC 262400835.